AN ABSTRACT OF THE THESIS OF

Kevin J. Drost for the degree of Honors Baccalaureate of Science in Mechanical Engineering presented May 21, 2010. Title: Direct Numerical Simulation of a Flat Wing with a Movable Front Flap at High Angles of Attack and Low Reynolds Numbers.

Abstract approved:

_____

Sourabh Apte

Low Reynolds number airfoils have become of interest recently for applications on Micro-air Vehicles (MAVs). Airfoils at low Reynolds numbers and high angles of attack are known to be unstable due to low lift to drag ratios. This study investigates the effect of a movable leading edge flap on the lift to drag ratio of an airfoil for use on MAVs. Direct numerical simulation (DNS) is used to fully resolve the flow around a thin airfoil at high angles of attack. The airfoil is represented numerically using a fictitious domain approach and assuming two-dimensional flow. The solver is validated using the standard case of a cylinder in cross-flow. Preliminary experimental data for the lift of the airfoil compares well with the numerical results for two angles of attack. Cases were run at a Reynolds number of 14,700 and an angle of attack of 20 degrees to study the effect of the front flap at a static angle and the effect of an oscillating front flap. Lowering the front flap to an angle of 20 degrees increased the lift to drag ratio to 5.84 compared to 2.47 for the no flap case. Cases with a moving front flap were run at 1, 3, and 5 Hz. The flapping motion caused the time-varying lift coefficient to become more predictable and periodic. The presence of lift and drag fluctuations is found to depend on how vortices are shed from the leading edge of the airfoil.

Key Words: Micro-air vehicle, Low Reynolds number, DNS, Fictitious Domain

Corresponding e-mail address: drostk@onid.orst.edu

Direct Numerical Simulation of a Flat Wing with a Movable Front Flap at High Angles of Attack and Low Reynolds Numbers

by

Kevin J. Drost

A PROJECT

submitted to

Oregon State University

University Honors College

in partial fulfillment of
the requirements for the
degree of

Honors Baccalaureate of Science in Mechanical Engineering (Honors Associate)

Presented May 21, 2010
Commencement June 2010

Honors Baccalaureate of Science in Mechanical Engineering project of Kevin J. Drost presented on May 21, 2010.

APPROVED

_____

Mentor, representing Mechanical Engineering

_____

Committee Member, representing Mechanical Engineering

_____

Committee Member, representing Mechanical Engineering

_____

Head, School of Mechanical, Industrial, and Manufacturing Engineering

_____

Dean, University Honors College

I understand that my project will become part of the permanent collection of Oregon State University, University Honors College. My signature below authorizes release of my project to any reader upon request.

_____

Kevin J. Drost

ACKNOWLEGEMENTS

I would like to thank my project mentor Dr. Sourabh Apte for his time and effort. Without his patient guidance this thesis would not have been possible. A special thanks to Justin Finn for his general help with computer programming and help troubleshooting the solver.

TABLE OF CONTENTS

LIST OF FIGURES

LIST OF TABLES

LIST OF APPENDICES

LIST OF APPENDIX FIGURES

LIST OF APPENDIX FIGURES (cont.)

Figure Page

Direct Numerical Simulation of a Flat Wing with a Movable Front Flap at High Angles of Attack and Low Reynolds Numbers

1) INTRODUCTION

Background

Recently, there has been increasing interest in the aerodynamics of low Reynolds number airfoils. Low Reynolds number airfoils have applications in the development are of micro-air vehicles (MAVs). MAVs are typically compact and unmanned devices designed for surveillance, military, or remote sensing. Depending on the application, MAVs can be autonomous or piloted remotely. Removing the risk to a human also makes MAVs ideal for detecting radioactive or biological hazards.

These applications combined with advances in miniaturizing sensors have been a driving force to better understand the aerodynamics of small scale airfoils. Airfoils for MAVs can be characterized by the Reynolds (Re) number based on the free stream velocity (v_∞) and the chord length (c) of the airfoil. Figure 1 shows a possible airfoil design at an angle of attack (α) with a front flap of a given length (l_f) and flap angle (θ).

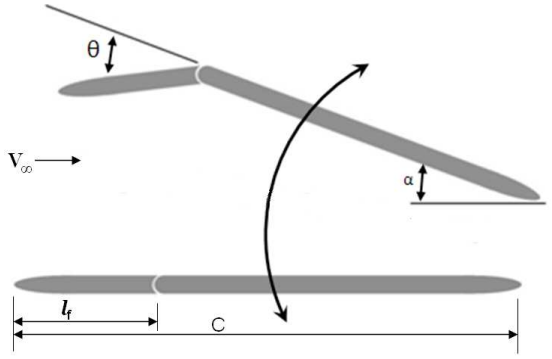

Figure 1: Schematic of a possible airfoil for a MAV.

Airfoils having a Reynolds number less than 10^5 are generally grouped as low Reynolds number airfoils. The Reynolds number dictates the general behavior of an airfoil. As the Reynolds number decreases, airfoils begin to exhibit different characteristics, some of which degrade performance.

How the boundary layer develops around an airfoil is one of the most important features in determining the performance of the airfoil. Additionally, the boundary layer characteristics are a strong function of the Reynolds number. Two common features of a boundary layer are flow separation and laminar to turbulent transition. Flow separation is caused by an adverse pressure gradient that forms a recirculation region near the surface of the airfoil. After flow separation, the laminar flow can transition to turbulent. The increased mixing in turbulent flow can cause the flow to reattach to the airfoil. For Reynolds numbers between 10,000 and 70,000 Carmichael [1] found that once flow separates, the turbulent transition will not occur in time to allow the flow to reattach to the airfoil. At higher angles of attack, flow separation causes a large recirculation zone that can cover the upper surface of the airfoil. This recirculation decreases airfoil performance and is generally called stall. In order to generate enough lift at low airspeeds, MAVs need to operate at higher angles of attack which make MAVs vulnerable to stall.

The stall angle of attack can be increased by adding camber to the airfoil. Camber is defined as the difference between the midline of the airfoil and the line that connects the leading and trailing edges. Camber can be increased through changing the cross-section of the airfoil or by the addition of a flap. There are many different types of flaps.

This investigation focuses on an airfoil with a leading edge flap. The camber of this airfoil can be increased by rotating the front flap downward (see Figure 1).

At higher angles of attack, the lift and drag coefficients of airfoils have some time dependency as turbulence from the leading edge moves across the upper side of the airfoil. These fluctuations can show a dominant frequency depending on how the turbulence occurs, specifically, how separated vortical structures travel down stream. This frequency can be characterized by its Strouhal number based on the free-stream velocity (v_∞) and the projected height of the airfoil, ($h = csin\alpha$).

$$St = \frac{fh}{v_\infty} \tag{1}$$

The performance of a flat airfoil with a leading edge flap was investigated in this study. It is expected that the numerical study will show that the addition of a front flap will increase the lift to drag ratio of the airfoil. Additionally, it is expected that by oscillating the front flap, the lift and drag of the airfoil should become periodic by matching the flap frequency. The computer model is based upon an actual airfoil produced by Kapsenberg et al. [2]. The chord length is 20cm with the leading edge flap making up 30% of the chord length. The airfoil thickness is 7.6mm and the leading and trailing edges are elliptical. Each ellipse has a length to height ratio of five. Two dimensional numerical results from this study are validated against two dimensional experimental data for the overall lift of the airfoil collected by Kapsenberg [3].

This numerical study uses a direct numerical simulation (DNS) solver for incompressible fluids. In DNS, the Navier-Stokes equations are solved on a fine grid resolving all length and time scales associated with the flow. DNS uses no turbulence model and therefore can fully resolve the turbulence around the airfoil. While

computationally expensive, DNS offers insight into how turbulence develops and its effects on the performance of the airfoil. In the present DNS study, the incompressible Navier-Stokes equations are solved using a finite volume approach and a pressure Poisson equation to appropriately correct the pressure and velocity fields to satisfy continuity. The solver is time accurate and can model moving rigid bodies through a hybrid Lagrangian-Eulerian (HLE) approach. In time, a fractional step method allows the solver to resolve the dynamic aerodynamic properties of rigid bodies. These rigid bodies are modeled as a collection of Lagrangian points that have user prescribed velocities. The rigid body motion is imposed over a Cartesian background mesh using a fictitious domain approach. Rigid body motion is enforced inside the rigid body through the addition of a force density term to the Navier-Stokes equation. The no-slip boundary condition is applied in bands of cells surrounding a rigid body.

Literature Review

Numerical and experimental work has been done to characterize the dynamic behavior of airfoils at low Reynolds numbers. Broeren and Bragg [4] studied the oscillations in lift for thin airfoils at angles of attack near stall at Re = 300,000. The oscillations in lift increased dramatically as the airfoils reached stall. Also, the Strouhal number for the dominant oscillations was shown to be a strong function of angle of attack. Broeren and Bragg reported that the magnitude of lift oscillations depends on the which of three types of stall occurs, leading edge, trailing edge, or thin airfoil stall. Some of the largest oscillations occurred with a combination of stall types. The stall types were first identified by McCullough and Gault [5].

Uranga et al. [6] recently conducted Large Eddy Simulations of stationary airfoils at low Reynolds numbers using a high-order Discontinuous Galerkin method on a body fitted grid. These simulations were for three dimensional airfoils at low angles of attack. The Re = 10,000 case showed that the flow remained essentially two dimensional over the airfoil surface. Schlüter [7] has done experimental work with asymmetric airfoils at low Reynolds numbers. The experiments studied the effect of a flap mimicking how a bird uses its feathers at high angles of attack and found that the addition of a rear flap increased the lift of an airfoil. The experimental work was done in a water tunnel at Re = 30,000 and 40,000.

Taira and Colonius [8] conducted numerical studies of flat-plate airfoils beyond stall at ultra-low Reynolds numbers of 300 and 500 and found that the coefficient of lift and drag could show a dominant frequency of oscillation depending on the angle of attack. The frequencies were found to be around $St_h = 0.14$ depending on the Reynolds number. Morse and Liburdy [9] have done experimental work to evaluate how vortices are shed from flat wings at high angles of attack for a Reynolds number of 14,700. They found that the shear region near the leading edge has a dominant frequency corresponding to a $St_h = 3.4$. The Strouhal number increased with both angle of attack and Reynolds number. In the recirculation region, low frequency oscillations have the largest amplitudes with no dominant frequency.

Visbal et al. [10] conducted extensive simulations of airfoils at low Reynolds numbers. These simulations used a finite difference method and a body fitted grid with compressible flow formulation. The study showed how the flow transitions from laminar to turbulent for low angles of attack and then develops into full flow separation around

the stall angle. These simulations were run at a Reynolds number of 60,000. Simulations were also run at an angle of attack of eight degrees for a variety of Reynolds numbers. The larger Reynolds number cases transitioned to turbulent flow quickly and showed little flow separation. The lower Reynolds number cases had larger flow separation. Visbal et al. [10] also simulated an airfoil going through a plunging motion. This study showed that flow remained mostly two dimensional for a Reynolds number of 10,000. For low-speed flows, use of a compressible formulation severely limits the time-step based on the speed of sound. An incompressible flow solver capable of handling arbitrary shaped moving rigid bodies is advantageous.

The numerical technique used in this study was developed by Apte et al. [11]. This method uses a fictitious-domain approach to model incompressible fluids interacting with rigid particles. The fluid and particles can be different densities. The fluid region is constrained by the continuity equation and the particle region is constrained to undergo rigid body motion. Finn [12] continued to develop the fictitious domain approach into the HLE scheme used in this investigation. While Finn's work was directed at bubble vortex interaction, Finn also validated the HLE method for many different types of rigid bodies including a hydrofoil at Re = 2000. This study uses the same solver as Finn's work.

2) NUMERICAL IMPLEMENTATION

Overview of Numerical Scheme

This section provides an overview of the numerical schemes used in the solver. For a complete and rigorous explanation see Finn's derivation of the HLE technique [12] and Apte et al. fictitious domain technique [11].

Fundamentally, the solver works by taking the computational domain and discretizing it into many control volumes (CVs). Each CV is constrained by conservation of momentum and mass. The fluid of interest in this case is air. For low Mach numbers (< 0.3), air can be assumed to be incompressible. The Navier-Stokes equations represent conservation of momentum for a Newtonian fluid, and is given as

$$\rho\left(\frac{\partial \overline{v}}{\partial t}+\overline{v}\cdot\nabla\overline{v}\right)=-\nabla P+\nabla\cdot\left(\mu\nabla\overline{v}\right)+S\,, \tag{2}$$

where ρ is the fluid density, $\overline{v}$ is the velocity vector, P is the pressure, μ is dynamic viscosity, and S is an additional momentum source. For an incompressible fluid, Equation 3 represents conservation of mass, also referred to as the continuity equation.

$$\nabla\cdot\overline{v}=0 \tag{3}$$

A distinguishing factor among fluids solvers is how the domain is broken up into CVs. For flow around objects, one way is to make a body-fitted grid where the faces of the CVs are aligned with the surface of the object. This method can be efficient for static objects. However, this study requires the solver to be able to handle moving objects. For moving objects, body-fitted grids become more computationally expensive. Each time the object moves, the grid must be regenerated and the flow variables interpolated onto the

new grid. These steps create computational cost and can introduce error. For these reasons, this study used a fictitious domain approach.

In the fictitious domain method, the entire computational domain is discretized into a static background grid. The Navier-Stokes and continuity equations are solved over the entire domain. Parallel processing is used to divide the computation among multiple processors. Objects are introduced into the domain by constraining the fluid velocity inside the object to the rigid body velocity of the object through the addition of a force density term to the Navier-Stokes equations. The object is assumed to be a rigid body, meaning the body's velocity is the sum of translational and rotational motion. This method requires a way to track what CVs are inside of an object. The HLE method tracks the surface of a rigid body using Lagrangian particles.

These Lagrangian particles or material points start at user defined locations in the shape of the immersed object. At each time step, the material points are moved to a new location based on their velocity. As the material points move, so does the surface of the object. The solver defines the surface of the object by tagging the CVs that contain material points. These CVs create a band. The solver then creates two additional bands consisting of the CVs adjacent to the first band. Figure 2 shows a two dimensional representation of the banded approach. By using three bands, the solver smears the interface between object and fluid. To account for this, a color function can by calculated. Inside the object, the color function is one; outside the color function is zero; and inside the banded region the color function is some fraction of one. The color function scales whether the CV is constrained to rigid body motion or not. The fact that this rigid body

constraint is smeared over multiple CVs requires that the grid always be refined near the surface of the object.

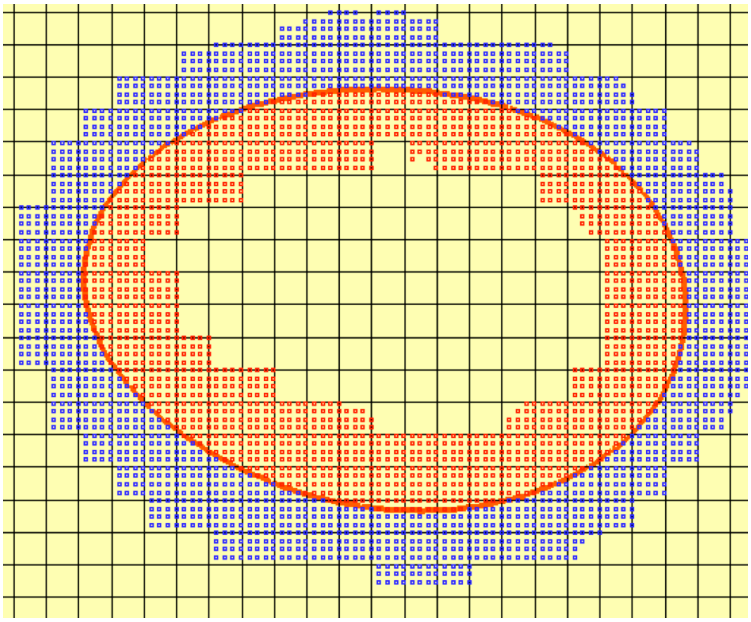

Figure 2: Banded approach for an arbitrary object.

Variable Storage and Solution Algorithm

The flow variables are stored at the center of each CV in accordance with a collocated arrangement with the exception of the face-normal velocities which are stored at the face centers. While this study uses structured grids, a collocated arrangement makes the solver more adaptable to unstructured grids. Figure 3 shows a diagram of the variable storage and time discretization. The variables are staggered in time with the CV velocities (u_i), face centered velocities (u_N), particle velocities (U_i), and rigid body forces ($f_{i,R}$) known at each time step and the pressure (p), particle position (X_i), density (ρ), and volume fraction (Θ) known at each half time step. This staggering has the advantage of

making the time discretization symmetric which helps the conservative properties of the numerical scheme.

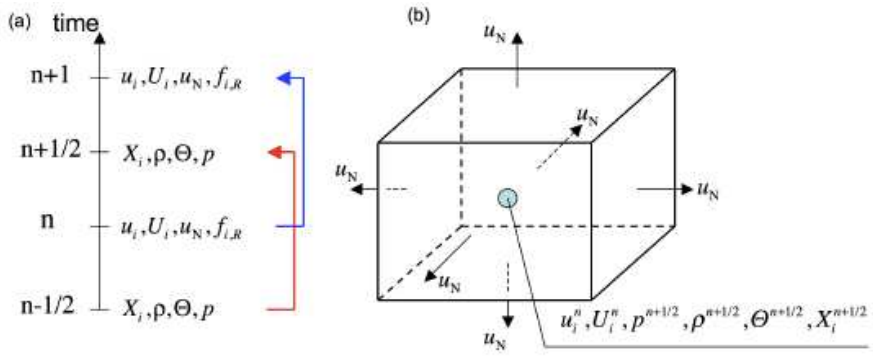

Figure 3: Diagram of variable storgae: (a) Time staggering, (b) three dimensional variable storage.

The following solution sequence is a summary of Finn's description of the HLE algorithm [12]. The solution algorithm begins with initial conditions for all flow variables and material point positions. First the material points are explicitly advanced in time based on the rigid body velocity. With the new material point positions, the color function is calculated over the entire domain. Next the velocities are advanced in time using the fractional step method. The result is a predicted velocity field that may not satisfy continuity. Velocity gradients are handled implicitly using the Crank-Nicholson method and spatial gradients use the centered discretization scheme.

Next, the pressure is solved for in a Poisson equation. With the new pressure values, the face-centered velocity field can then be corrected to satisfy the continuity equation. Finally, the CV velocities inside the object are corrected to meet the rigid body constraint. This requires the user to specify the translational and rotational velocities of the rigid body.

Airfoil Model

In order to run simulations on an airfoil, first a computational model must be generated. This study models an existing thin airfoil with a front flap. The trailing and leading edges are rounded into an elliptical shape with a length to height ratio of five. The chord length is 20cm, the thickness is 7.6mm, and the front flap makes up 30% of the chord length. Figure 4 shows the actual airfoil that the numerical model simulates.

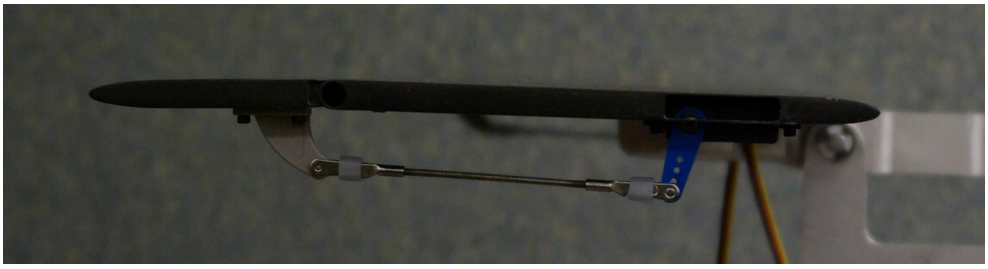

Figure 4: Side view of the actual airfoil built by Kapsenberg et al [2].

The numerical model of the airfoil was created by distributing material points along the surface of the airfoil. The airfoil surface was defined by breaking the airfoil up into simple shapes. The entire airfoil is generated at an angle of attack of zero with a flap angle of zero. The material points are then rotated to the appropriate angle of attack. The five component shapes are an ellipse for the trailing edge, a line segment for the body of the airfoil, a semicircle for the hinge joint, a line segment for the flap body, and an ellipse for the leading edge. The origin for the airfoil is located at the trailing edge with the front of the airfoil pointed to the left (negative x direction). Due to the symmetry of the airfoil, for each point placed on the top surface of the airfoil, another is placed on the bottom surface by mirroring the top point across the x-axis. The airfoil is given depth by copying the points from the first cross-section to make additional cross-sections in the z direction.

The ellipses for the leading and trailing edges are generated using the general equation for an ellipse, the thickness of the airfoil, and the ratio of length to height. Equation 4 shows the equation that can be solved for the y location of a point on an ellipse centered on the x-axis,

$$\frac{\left(x-x_c\right)^2}{\left(\frac{1}{2}rt\right)^2}+\frac{y^2}{t^2}=1, \tag{4}$$

where x_c is the x location of the center of the ellipse, t is the thickness of the airfoil and r is the ratio of length to height. The x locations of the material points are spaced evenly between the tip of the ellipse and the center. The y location is solved for using Equation 4. The x_c for the trailing edge and leading edge are ($-t*r / 2$) and ($t*r / 2$ – c) respectively where c is the chord length.

Next the flat airfoil and flap sections are added. Each flat section is generated by equally spacing material points along the flat surface. The airfoil flat surface extends from the end of the trailing edge ellipse to the start of the flap hinge. The flat flap surface extends from the flap hinge to the end of the leading edge ellipse.

At this point the airfoil and flap are both horizontal. The next step is to rotate the flap to the specified flap angle. The flap angle is defined as positive counterclockwise. Each material point in the flap is rotated around the flap hinge using a matrix transformation.

Next the hinge material points are added. The hinge's height and width are equal to the thickness of the airfoil. The hinge is formed by fitting two semi-circles into the gap between the airfoil surface and the flap surface. The semicircles are created tangent to both the flap and airfoil surfaces to create a smooth transition. The upper and lower

semicircles are concentric. While adding the semi-circle to the underside of the airfoil does not match the shape of an actual hinge, the benefit is that the front flap can be moved smoothly without the need to add material points. The final step is to rotate all the material points around the trailing edge by the specified angle of attack. Angle of attack is defined as positive counterclockwise. Figure 5 shows how the material points are distributed to create a cross-section of the airfoil. In practice many more material points are used to more accurately define the interface

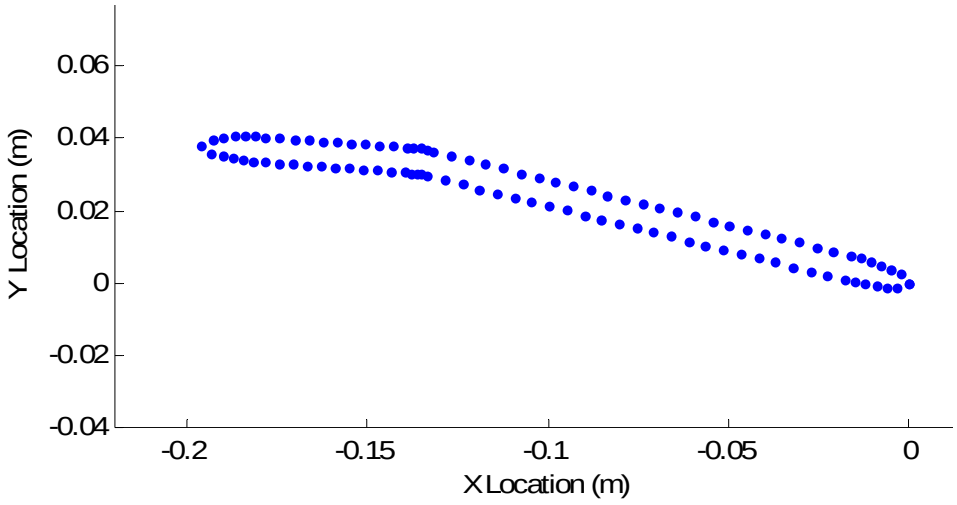

Figure 5: Diagram of material point distribution.

Figure 6 shows a contour plot of the volume fraction of the airfoil. The volume fraction varies between unity inside the airfoil and zero outside. At the interface between the airfoil and fluid, the volume fraction is smeared over three control volumes which accounts for the blurring of the airfoil edges in Figure 6.

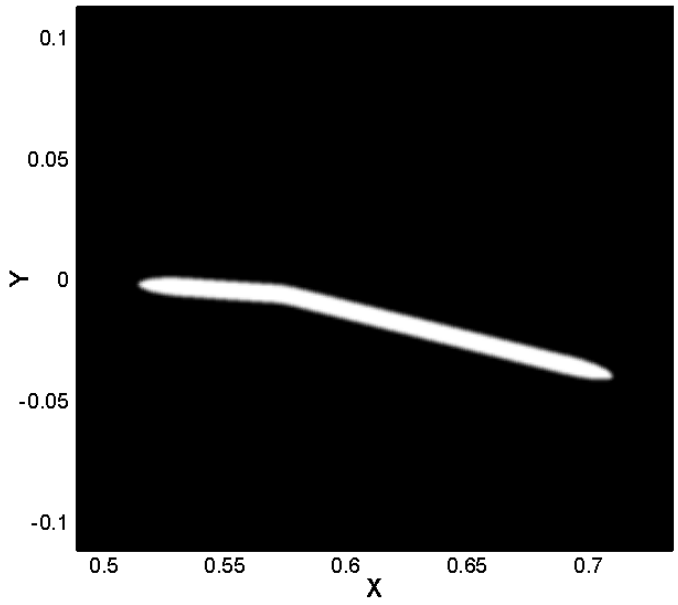

Figure 6: Plot of volume fraction contours for the airfoil model.

Figure 6 was generated on a coarse background grid. The blurring of the airfoil surface can be reduced by refining the grid in the region of the airfoil. The boundary of the airfoil is defined by the surface with a volume fraction of 0.5.

3) VALIDATION

Flow Past A Cylinder

The solver is validated by simulating flow past a cylinder at Reynolds numbers of 100 and 300 based on the cylinder diameter. These Reynolds numbers provide coefficients of drag and frequencies of vortex shedding that can be compared to previous simulations. The computational domain is a 256 X 256 X 3 Cartesian grid. The flow is assumed to be two dimensional. The cylinder is three cells wide and has periodic boundary conditions to ensure a two dimensional flow. The grid is refined in the region of the cylinder with 24 CVs across the diameter of the cylinder. A cross-section of the grid is square with sides equal to 32 cylinder diameters. The upper and lower surfaces have slip wall boundary conditions; the left side has a velocity inlet boundary; and the right side has an outlet boundary. See Appendix A for diagrams of the computational domain.

At a Reynolds number of 100, the wake of a cylinder is known to be two dimensional and develop periodic vortex shedding. Equation 5 shows the definition of a lift or drag coefficient.

$$C = \frac{F}{\frac{1}{2}\rho U^2 A} \tag{5}$$

F is the force to be non-dimensionalized; ρ is the density of the fluid; U is the free stream velocity; and A is the characteristic area or the length times the diameter of the cylinder. Figure 7 shows how the lift and drag coefficients develop over time. Time is non-dimensionalized by multiplying by the free stream velocity and dividing by the diameter of the cylinder.

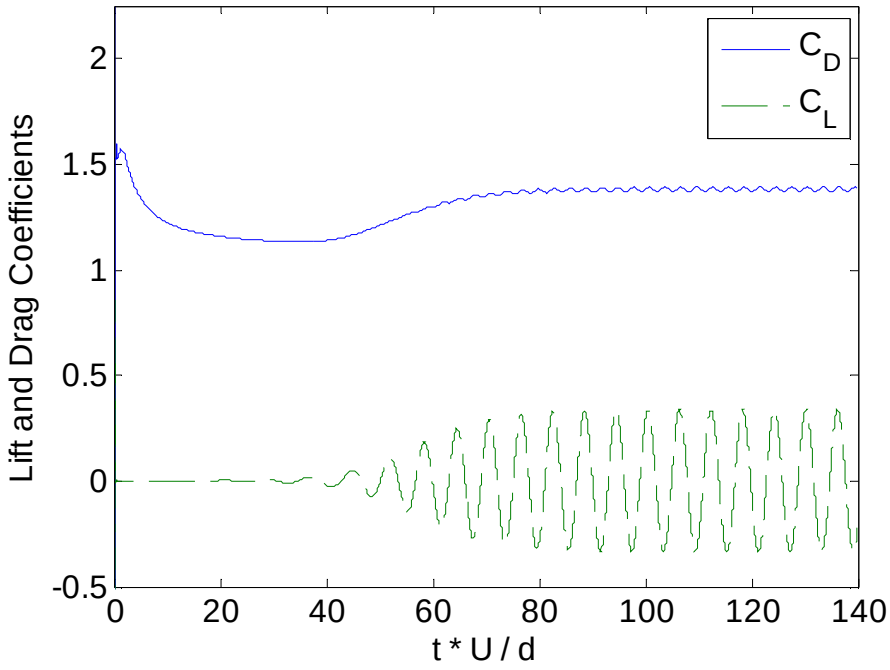

Figure 7: Time evolution of lift and drag coefficients, Re = 100.

Over time the cylinder develops the characteristic oscillations in both lift and drag. Since the cylinder is symmetric, the lift coefficient is centered about zero while the drag coefficient is centered about a positive value. After t * U / d = 80, the oscillations reach a steady amplitude and mean. The mean value for the drag coefficient is 1.38. Table 1 shows the drag coefficient compared to past work. The lift coefficient closely agrees with the other work. Additionally, the Strouhal number can be calculated for the frequency of lift oscillations using the diameter of the cylinder and the free stream velocity. Equation 6 shows the definition of the Strouhal number.

$$St = \frac{fd}{U}, \tag{6}$$

where f is the frequency; d is the characteristic length or the cylinder diameter; and U is the free stream velocity. The Strouhal number is 0.163. Table 1 compares this Strouhal number to past work and shows close agreement.

Table 1: Comparison of C_d and St for a 2D cylinder, Re = 100.

	C_d	St
Present Study	1.38	0.163
Mittal et al. [13]	1.35	0.166
Marella et al. [14]	1.36	-
Henderson [15]	1.35	-
Shu et al. [16]	1.3833	0.16

For the Re = 300 case, the same grid is used. At this Reynolds number, the wake behind the cylinder is known to be three dimensional. Therefore the two dimensional assumption will introduce some error. Figure 8 shows the coefficients of lift and drag over time. The lift and drag coefficients appear similar to the Re = 100 case. There is some transient behavior at the beginning before the coefficients reach steady state oscillations. The drag coefficient has a mean value of 1.43. The lift oscillations come out to a Strouhal number of 0.210. Both of these values are similar to past numerical results as seen in Table 2.

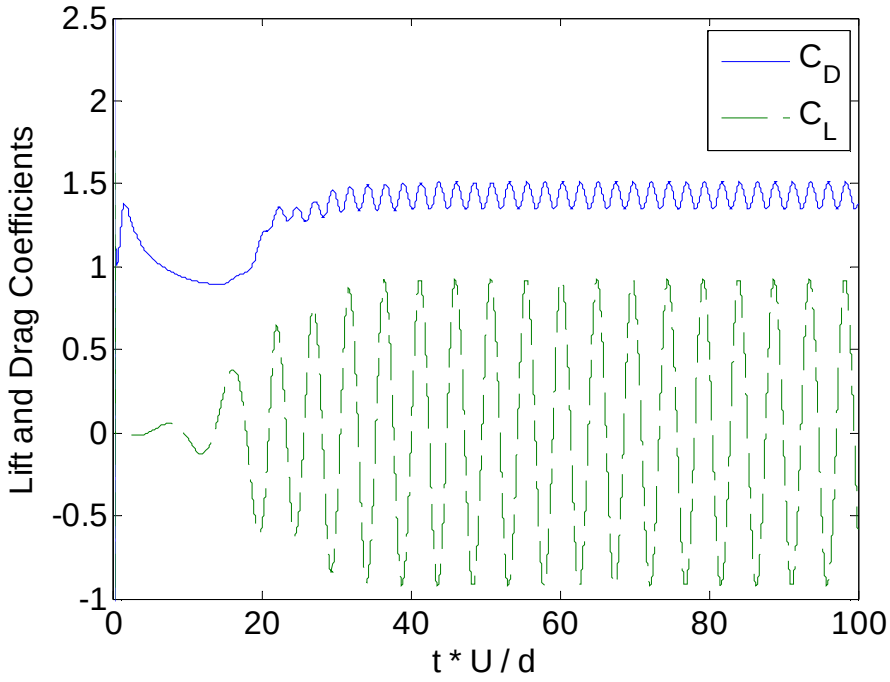

Figure 8: Time evolution of lift and drag coefficients, Re = 300.

Table 2: Comparison of C_d and St for a 2D cylinder, Re = 300.

	C_d	St
Present Study	1.43	0.210
Mittal et al. [13]	1.36	0.21
Marella et al. [14]	1.28	-
Mittal and Balachandar [17]	1.37	-
Henderson [15]	1.37	-
Kravchenko et al. (3D) [18]	-	0.203

Figure 9 shows vorticity contours around the cylinder for both cylinder cases. Qualitatively, the vorticity distributions for each case are consistent with periodic vortex shedding. The distance between vortices is slightly smaller for the Re = 300 case reflecting its slightly higher Strouhal number compared to the Re = 100 case.

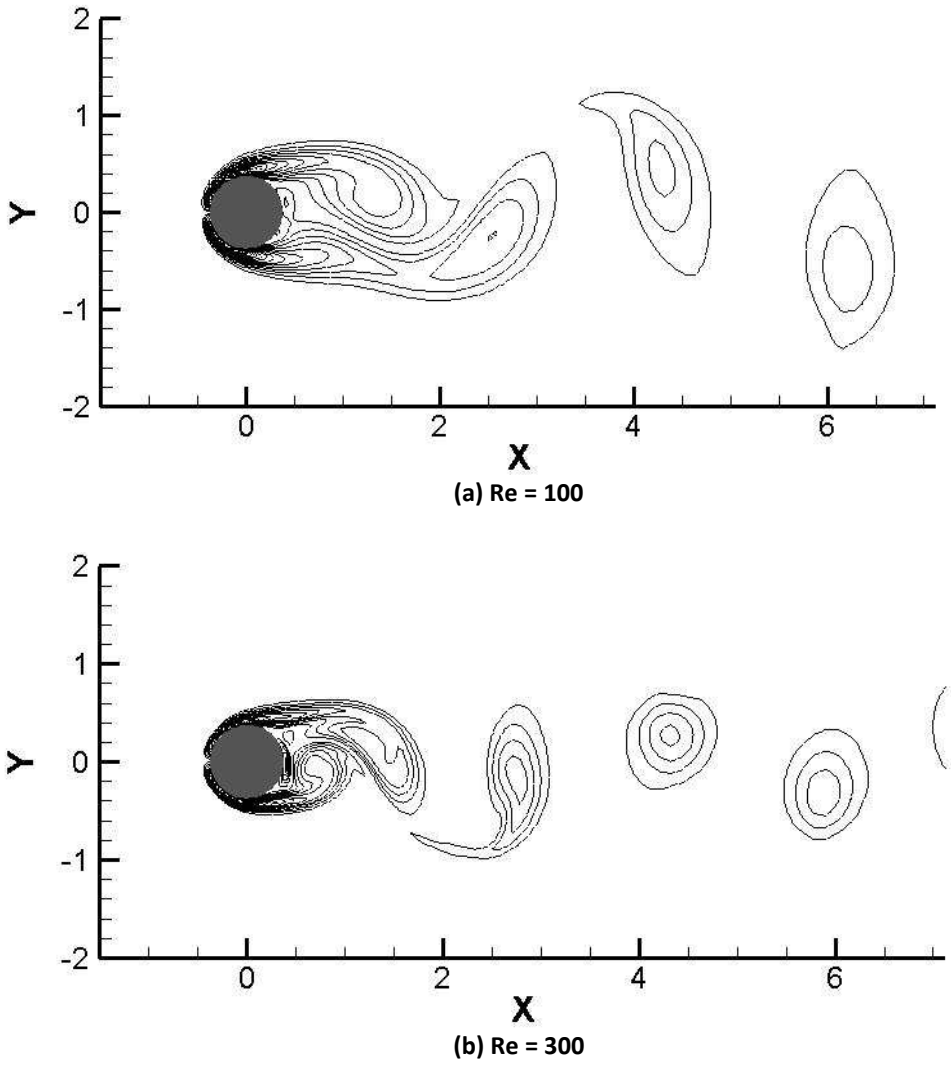

Figure 9: Vorticity contours around a cylinder at (a) Re = 100, (b) Re = 300.

Cylinder Grid Refinement Study

In order to determine an appropriate grid resolution for running airfoil cases, cylinder cases for a Re = 100 were run at different grid resolutions and compared. The computational domain was shrunk to 12 X 13 cylinder diameters to reduce computation time. Boundary conditions were the same except the top and bottom walls were no-slip walls. While no-slip walls are not good practice for getting realistic drag values, this

study is focused on the relative behavior between grid resolutions. The fine grid used 400 X 400 X 4 CVs and is assumed to be near to the true numerical solution. The cylinder is located near the center of the domain and is in a refined grid region. See Appendix B for diagrams of the grid distribution. This grid resolution places 75 CVs across the diameter of the cylinder. Two other cases were run with 18.8 and 9.4 CVs across the diameter of the cylinder. Figure 10 shows how the drag coefficient develops over time.

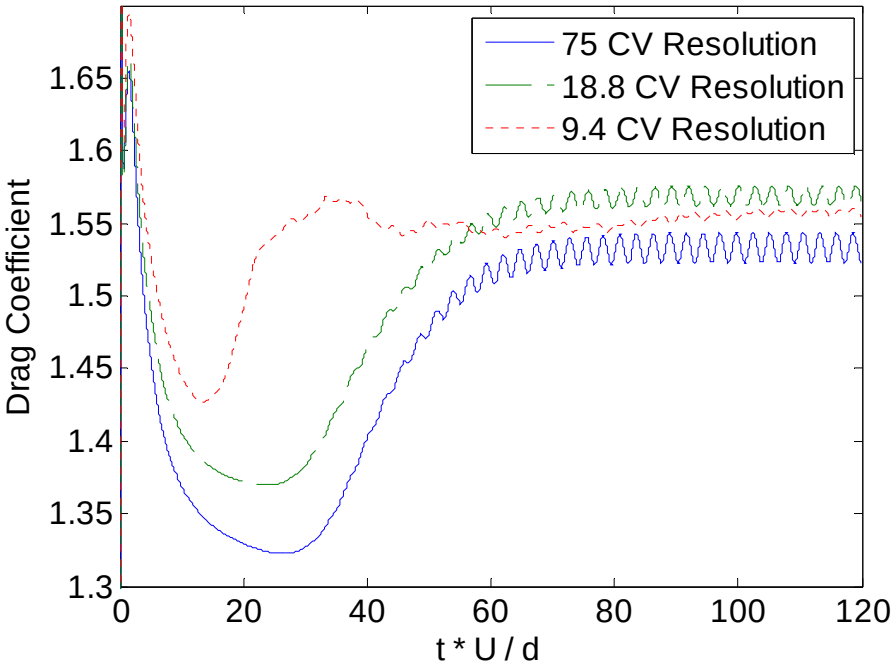

Figure 10: Drag coefficient over time for three different grid resolutions.

The mean coefficient of drag for the three grid refinements are 1.53, 1.57, and 1.56 in order of decreasing resolution. While the means agree closely, the transient behavior differs considerably. The 75 CV and 18.8 CV cases have one dominant frequency, while the 9.4 CV case has two significant frequency components. The 9.4 CV case also has a smaller amplitude of oscillation. The dominant frequencies for all cases

are similar with Strouhal numbers of 0.180, 0.189, and 0.200 in order of decreasing resolution. The effect of decreasing the grid refinement has a large impact on the results. Using a grid resolution of 9.4 produced satisfactory values for a mean coefficient of drag and Strouhal number, but the transient results became distorted.

4) RESULTS

Computational Domain for the Airfoil

The computational domain for the airfoil is setup to provide the required resolution around the airfoil while minimizing the total number of CVs used. The domain is two meters by two meters and is discretized into a Cartesian grid. The airfoil is centered vertically and slightly upstream of the center in the horizontal direction. The airfoil is in a refined region that is 0.24 m wide by 0.16 m tall. The refined region is large enough to always contain the airfoil and to resolve the important flow features. All CVs in the refined region are cubic.

Three different grid resolution are used, a coarse, an intermediate, and a fine grid. The three grids are 480 X 320, 720 X 480, and 840 X 560 in order of increasing refinement. All of the grids are three CVs wide in the spanwise direction which assumes that the flow is two dimensional. The left side is a velocity inlet boundary condition, the right side is an outlet, the top and bottom are no-slip walls, and in the spanwise direction, the boundary conditions are periodic. The coarse, intermediate, and fine grids have 7.6, 11.4, and 13.3 CVs across the thickness of the airfoil. See Appendix C for diagrams of the grids. While the coarse grid has insufficient resolution to obtain precise results, it can be used to get qualitative results. Even with parallel processing, the more refined grids are significantly more computationally expensive to run. In order to obtain satisfactory spectral resolution, cases needed to be simulated over longer time periods. These larger times add computational cost requiring the use of supercomputing facilities. In the present work, coarse grids were used for parametric studies. Even on a coarse grid, one

case takes approximately 1500 CPU hours to complete. Table 3 summarizes the results of the seven different cases.

Table 3: Summary of the lift and drag results for all seven cases.

Case	Re	α	θ	Flapping Frequency	Mean C_L	Mean C_D
1	70,000	10°	-10°	-	0.85	0.06
2	70,000	14°	-10°	-	1.16	0.19
3	14,700	20°	0°	-	1.38	0.56
4	14,700	20°	-20°	-	1.38	0.24
5	14,700	20°	-20°	1 Hz	1.47	0.31
6	14,700	20°	-20°	3 Hz	1.39	0.26
7	14,700	20°	-20°	5 Hz	1.37	0.22

Fixed Flap Angle Cases

The first two cases are of the airfoil with a constant flap angle and a Reynolds number of approximately 70,000. These two cases duplicate some preliminary experimental results collected by Kapsenberg [3] of the overall lift of the actual airfoil. The two cases have angles of attack of 10 and 14 degrees. Both cases use a flap angle of -10 degrees and the coarse grid. The experimental data is time averaged and eliminates tip effects by placing splitter plates flush with the sides of the airfoil. Figure 11 shows the transient numerical results for the coefficient of lift. Table 3 compares the experimental and numerical averaged lift coefficients. For the mean lift coefficient, the numerical results are time averaged starting after the initial transient. For both cases the numerical results are slightly higher than the experimental results. Since the experimental results are still preliminary, there is no reported uncertainty in the lift values. Therefore it is difficult to make a definite conclusion about the accuracy of the numerical results.

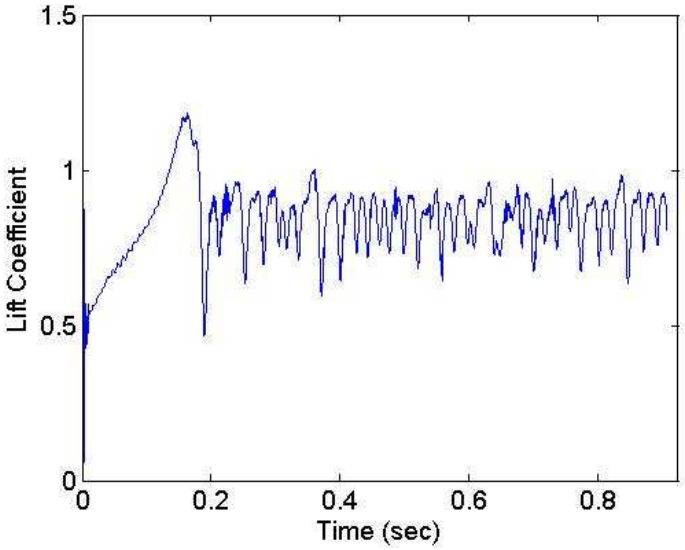

(a) Lift Coefficient for α = 10°, θ = -10°.

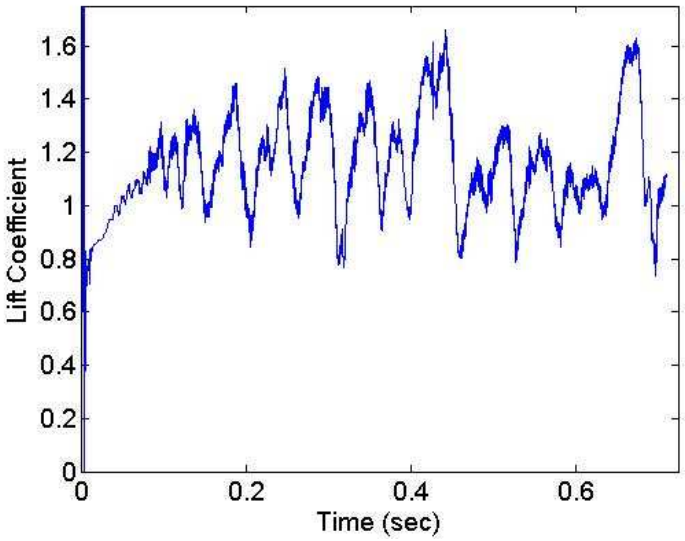

(b) Lift Coefficient for α = 14°, θ = -10°

Figure 11: Transient Lift Coefficient for the airfoil at two angle of attack on the coarse grid, Re = 70,000.

Table 4: Comparison of coefficient of lift for experimental and numerical studies of the airfoil for two angles of attack, θ = -10°, Re = 70,000.

Angle of Attack	Experimental Results [3]	Numerical Results
10°	0.79	0.85
14°	1.06	1.16

Two additional cases were run for the airfoil at a higher angle of attack to test the effect of the front flap. Both cases use an angle of attack of 20 degrees, but the flap is changed between -20 and 0 degrees. Both cases were run at a Reynolds number of 14,700. The zero degree flap angle case was run on the coarse, intermediate, and fine grids.

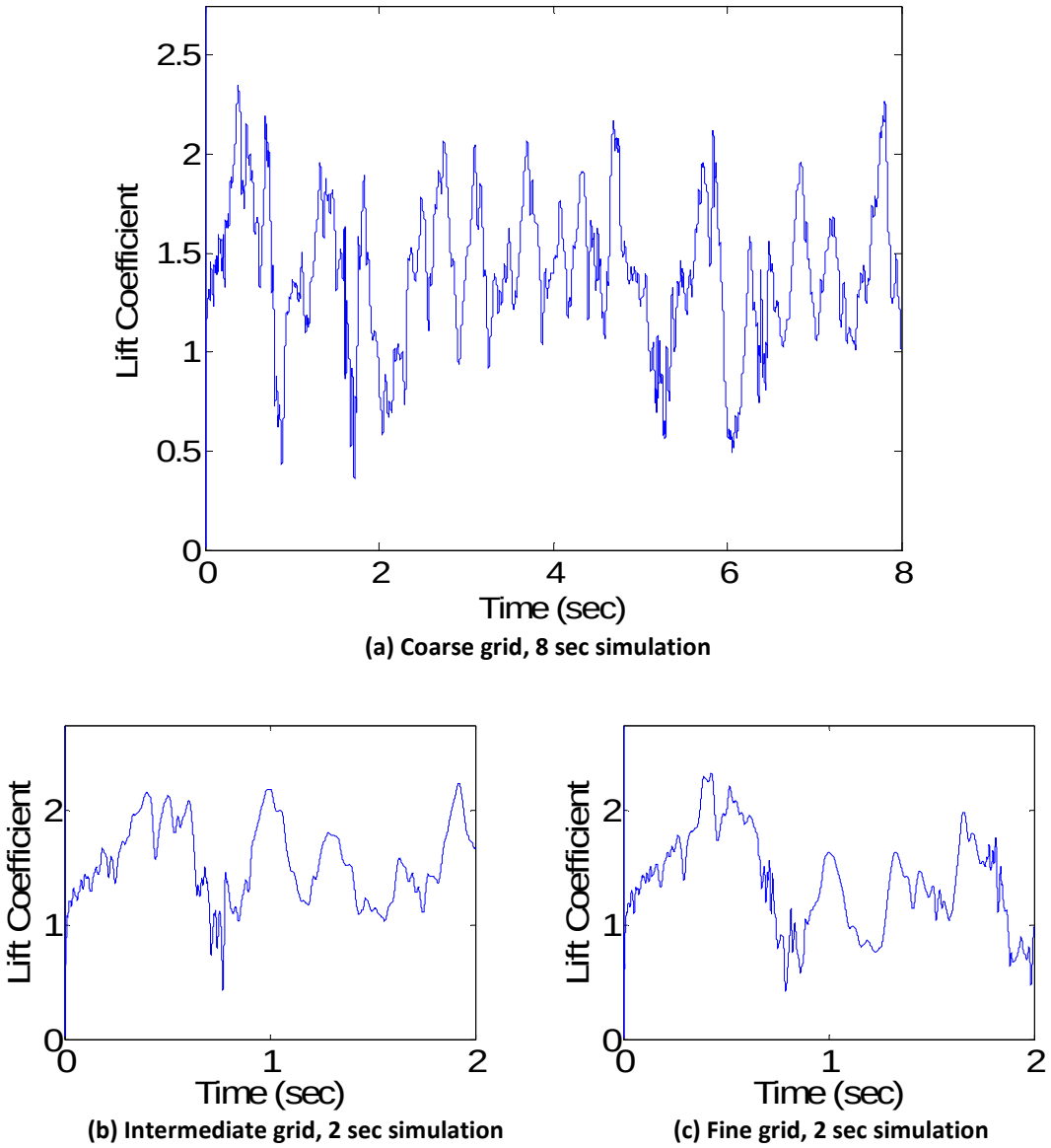

(a) Coarse grid, 8 sec simulation

(b) Intermediate grid, 2 sec simulation

(c) Fine grid, 2 sec simulation

Figure 12: Coefficient of lift for the airfoil, α = 20°, θ = 0°, Re = 14,700.

On all three grids, the lift coefficients begin to oscillate after an initial transient. The coefficient of lift varies significantly over time with extreme values of 2.26 and 0.36 on the coarse grid. Qualitatively, the lift coefficients for the three grids appear to be similar. However, the average lift values vary considerably from 1.38, 1.52, and 1.24 from the coarse to fine grid. When taking an average, the first second of results is discarded as the initial transient. Since this leaves only a second of data for the intermediate and fine grids, these averages might not reflect the true average over a long period of time. Generally, the coefficient of drag's oscillations are in phase with the coefficient of lift. For plots of drag data, see Appendix D. Figure 13 shows pressure contours around the airfoil. Vortices are generated in the shear regions above the leading edge and trailing edge. As these vortices interact and travel over the upper surface of the airfoil, the pressure differences change the overall lift and drag forces.

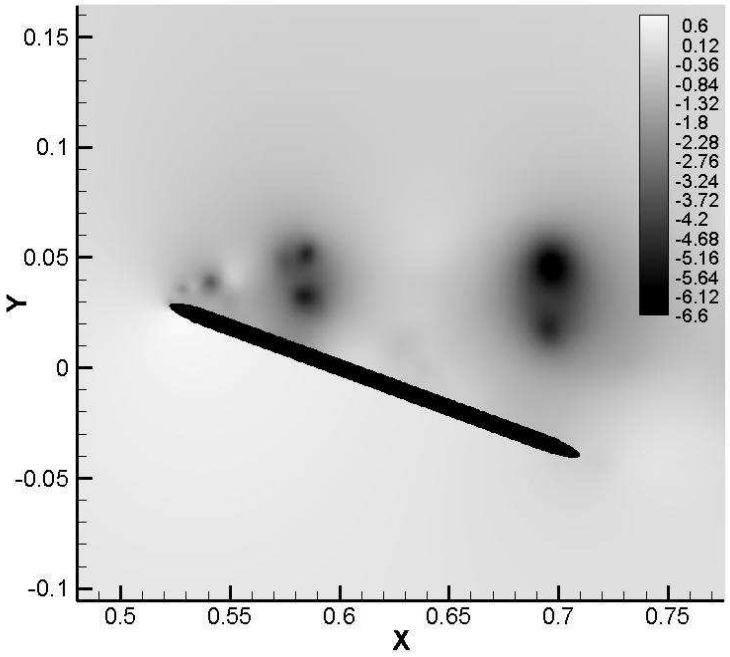

Figure 13: Pressure (Pa) contours around the airfoil, α = 20°, θ = 0°, Re = 14,700.

Similar cases were run for the airfoil at an angle of attack of 20 degrees with a flap angle of -20 degrees. Lowering the flap makes the flap parallel to the oncoming air and increases the camber of the airfoil. Figure 14 shows how the lift coefficient develops over time on the coarse grid. Pressure contours around the wing are plotted in Figure 15.

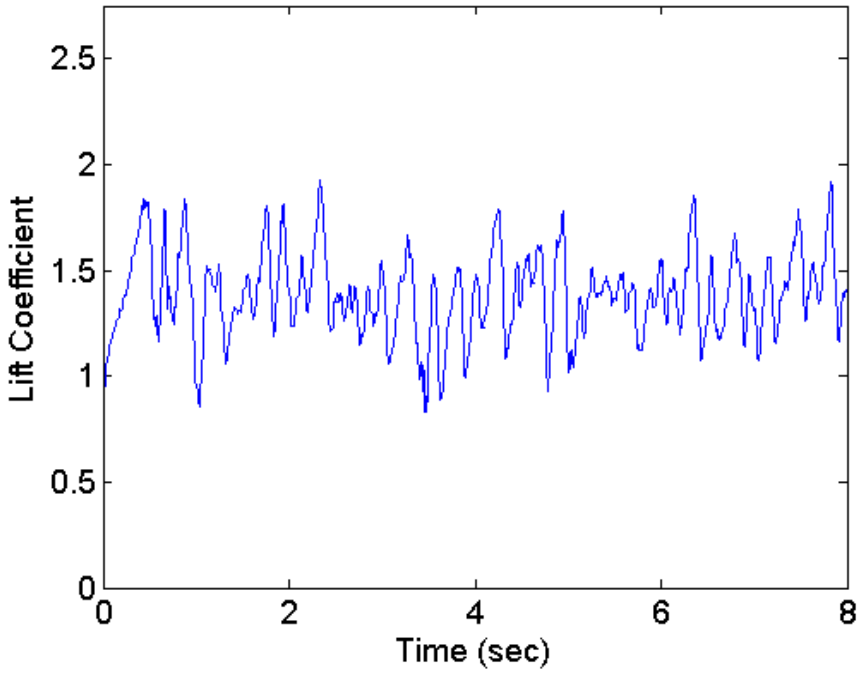

Figure 14: Coefficient of lift for the airfoil, α = 20°, θ = -20°, Re = 14,700.

The lift coefficient also oscillates as vortical structures pass over the airfoil. The average coefficient of lift is 1.38 and varies between extremes of 1.92 and 0.83. While the average coefficient of lift is identical between the θ = 0º and the θ = -20° cases, the θ = -20° case oscillates over a smaller range. To further compare the two cases, a spectral analysis was run on the two coefficient of lift signals. The amplitude of oscillation is plotted versus the Strouhal number in Figure 16.

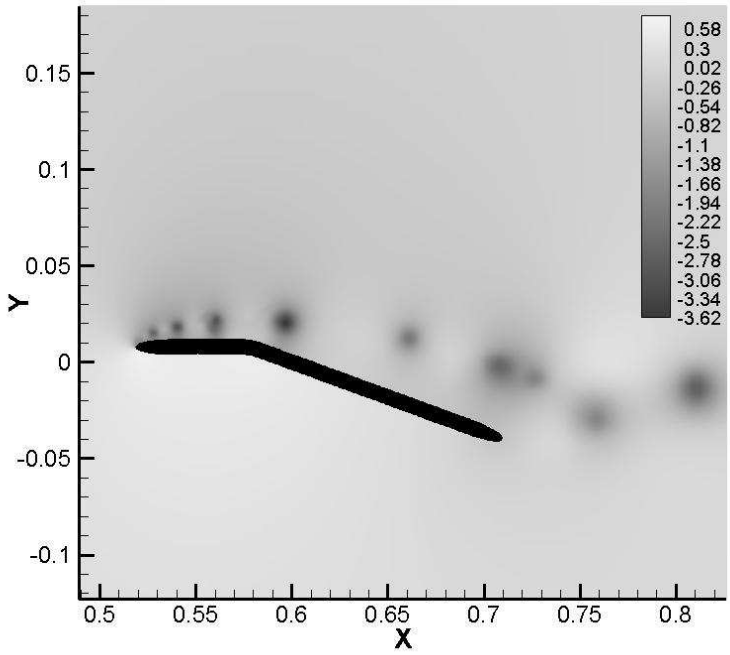

Figure 15: Pressure (Pa) contours around the airfoil, α = 20°, θ = -20°, Re = 14,700.

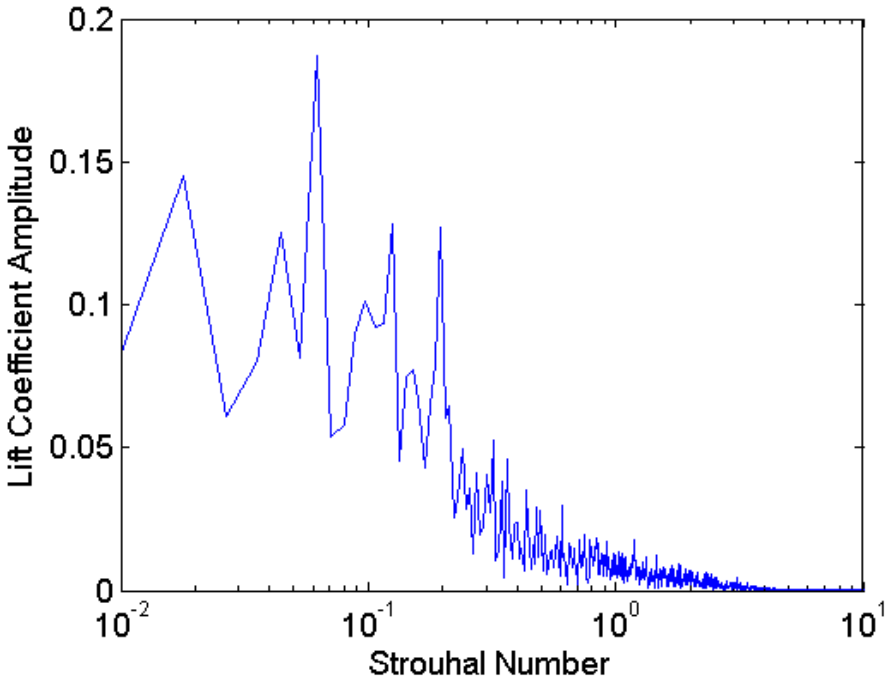

(a) θ = 0°

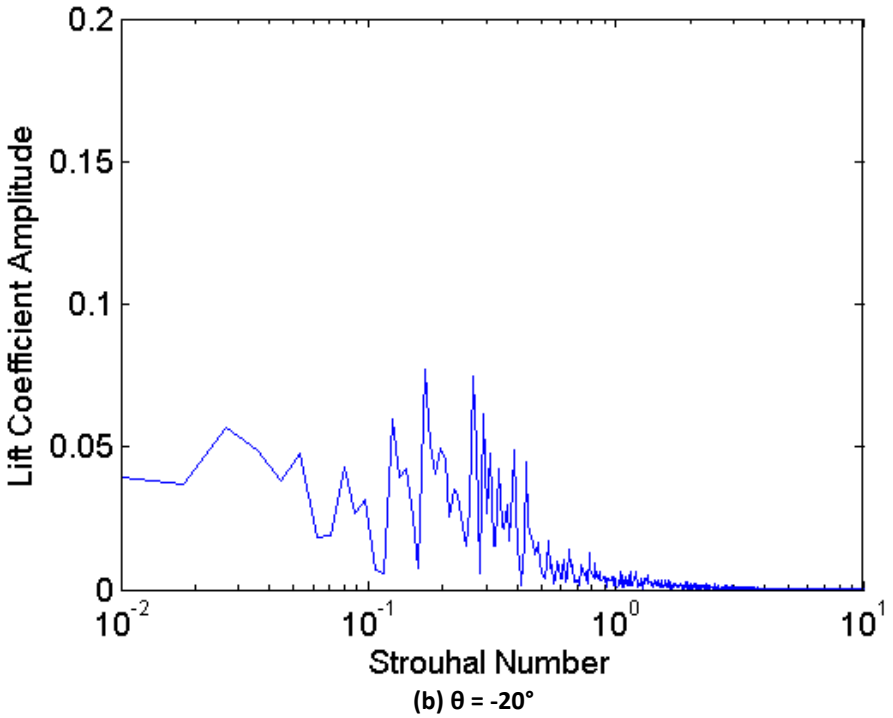

Figure 16: Spectral analysis of coefficient of lift for two flap angles, α = 20°, Re = 14,700.

The spectral analysis shows that the coefficient of lift is predominantly made up of low frequency oscillations. The θ = 0° case has much larger oscillations with a peak Strouhal number of 0.062 corresponding to a frequency of 1Hz. The θ = -20° case had a much smaller oscillations with a dominant Strouhal number of 0.17 or a frequency of 2.71 Hz.

Flapping Cases

Three additional cases were run with a moving flap at different frequencies, 1, 3, and 5 Hz. In each case, the flap angle oscillates sinusoidally with an amplitude of ten degrees and an average angle of -20 degrees. All three cases use the coarse grid. Figure

17 shows how the coefficients of lift vary over time. Plots of the drag coefficients are in Appendix E,

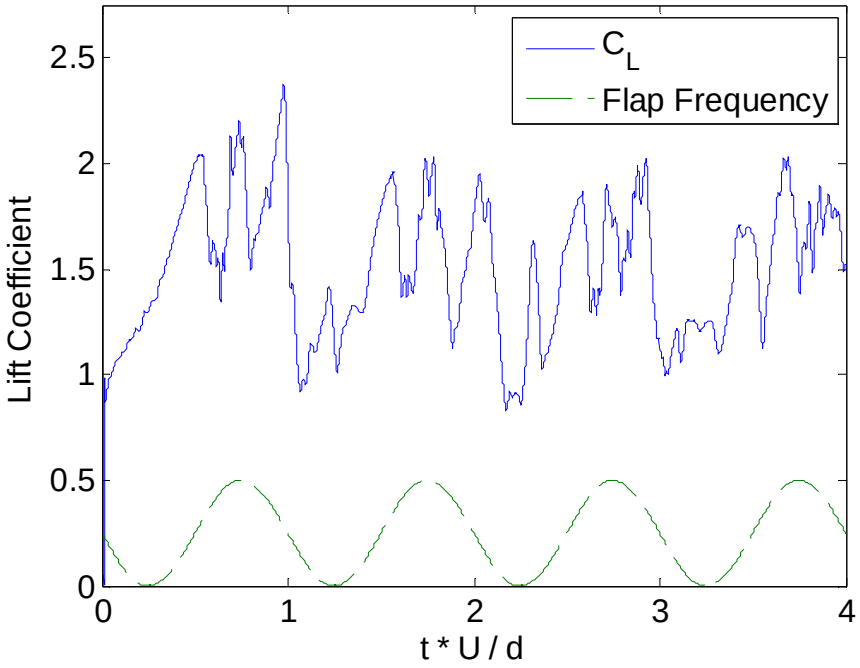

(a) Flap Frequency of 1Hz

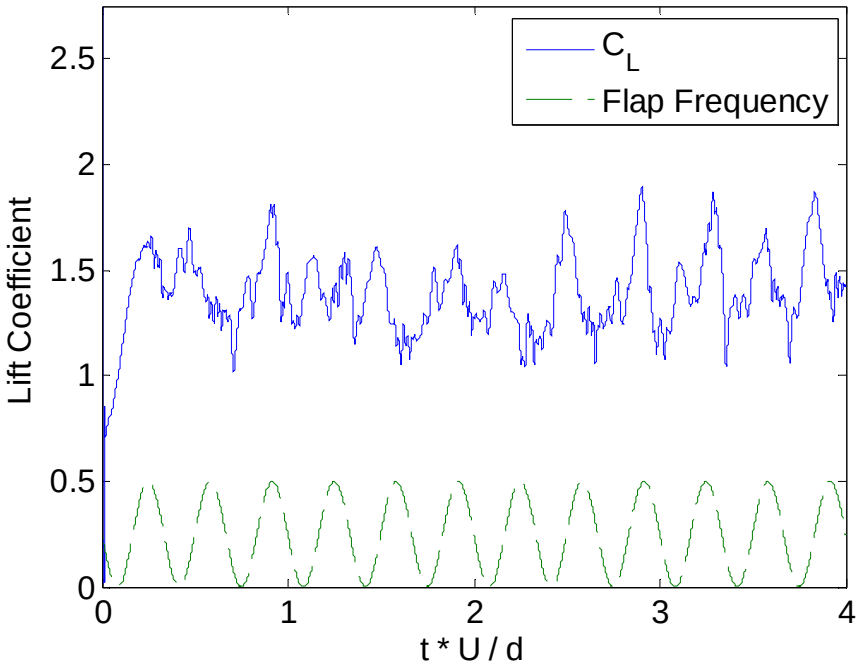

(b) Flap Frequency of 3Hz

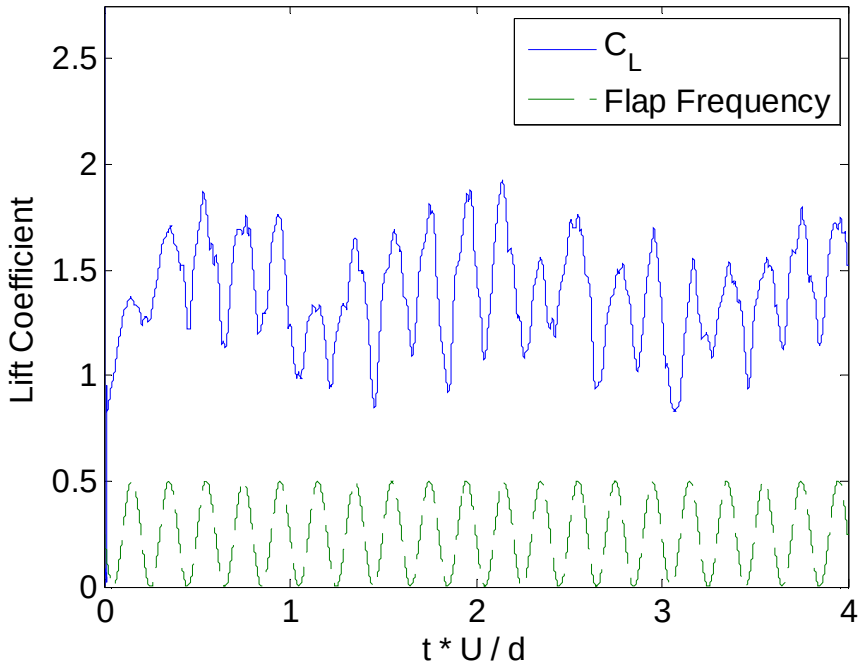

(c) Flap Frequency of 5Hz

Figure 17: Coefficients of lift for the airfoil with oscillating front flap angle at three different flapping frequencies.

For all three frequencies, the lift coefficient oscillations are in phase with the flap motion. The average lift coefficients for the 1Hz, 3Hz, and 5Hz cases are 1.47, 1.39, and 1.37 respectively. The average drag coefficients decrease with increasing flapping frequency and yield lift to drag ratios of 4.70, 5.33, and 6.36. Figure 18 shows the frequency content of the lift coefficient signals. All three signals have dominant frequencies equal to the flapping frequency. The 1Hz case also has oscillations of significant amplitude around a Strouhal number of 0.23 or 3.67 Hz. As the frequency increases, the lift coefficients become more sinusoidal with the 5Hz case having a large dominant frequency of 5Hz.

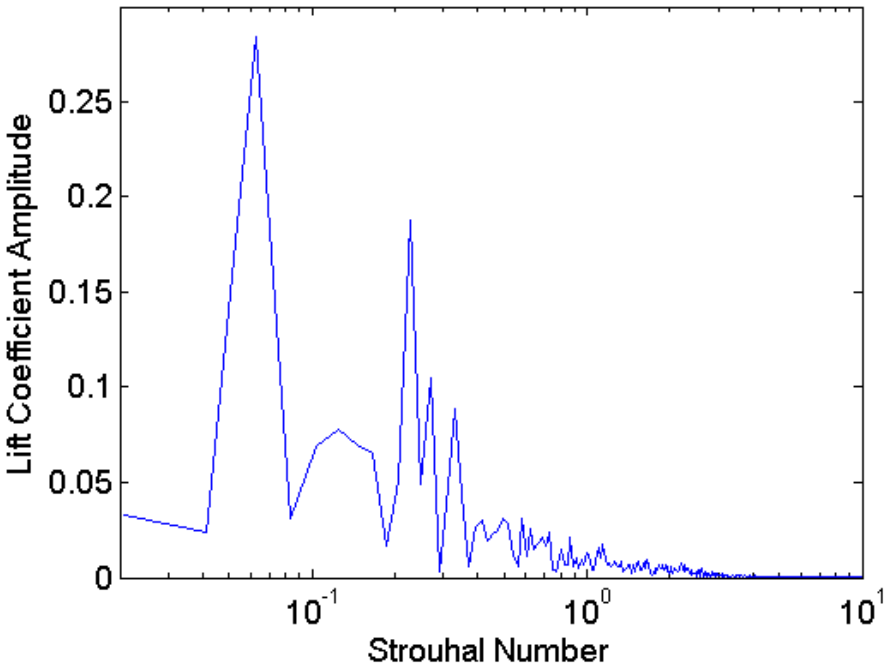

(a) Flapping frequency of 1Hz

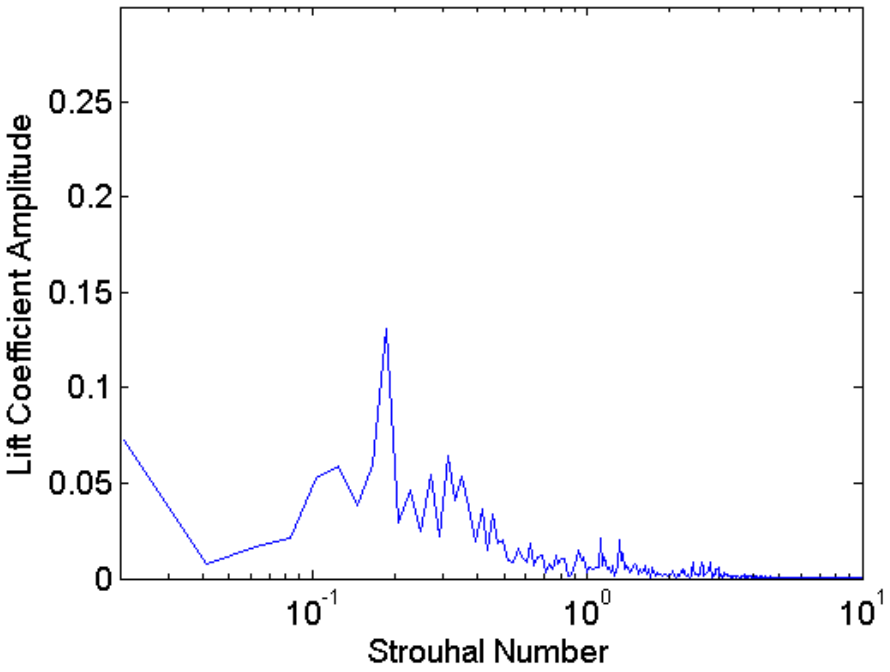

(b) Flapping frequency of 3Hz

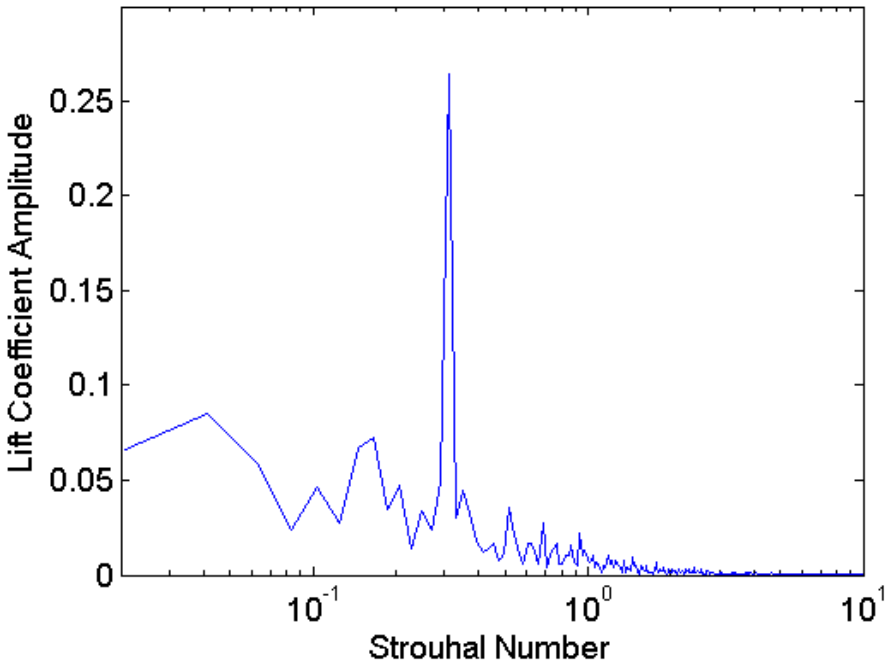

(c) Flapping frequency of 5Hz

Figure 18: Spectral analysis of the lift coefficient of the airfoil at three different flapping frequencies.

5) CONCLUSIONS

While the DNS simulations of the wing provided lift and drag coefficients that are close to the preliminary experimental results, more work needs to be done before the numerical methods can be conclusively verified. The cylinder grid refinement study demonstrated that coarse grids can provide results that are somewhat accurate, but more refined grids are needed to completely and quantitatively capture both the dynamic and the time averaged behavior of the rigid body. For cylinders, the appropriate level of grid refinement can be determined. However, it is still unclear what grid refinement is appropriate for the shape of a thin airfoil. Experimental results would be invaluable in determining the appropriate level of grid refinement for the airfoil shape. The present work assumes the flow over the airfoil is two dimensional. Three dimensional simulations or experimental results are needed to verify this assumption.

The results from the cases examining the effect of the front flap came out as expected. Lowering the front flap, provided significant increase in performance at a high angle of attack. While the coefficient of lift remained unchanged, the addition of camber by the flap decreased the coefficient of drag from 0.56 to 0.24. Additionally, the lift and drag oscillations were significantly reduced by lowering the flap. Reducing the oscillations in the airfoil, especially the lower frequencies, makes the airfoil more stable. With the addition of the flap, the largest oscillations shifted from a Strouahl number of 0.062 to 0.17. This data shows that lowering the flap by 20 degrees improved the performance of the airfoil. However, more simulations should be run to get a full understanding of the flap's effect. Cases of the flap at a larger variety of angles would show whether the improvements are smooth transition as the flap is lowered or if there is

a critical flap angle. There also should be an angle where lowering the flap further would degrade performance. Further studies are required to describe this angle. Simulations of greater length would also improve the resolution of the spectral analysis. Twenty seconds of data would better describe the dominant frequencies in lift and drag data.

As expected, the flapping cases showed that the motion of the flap significantly affected the nature of the lift coefficient. For all three flapping cases, the dominant frequency content in the lift and drag coefficients corresponded to the flapping frequency. The lift coefficient plots show that the lift was generally in phase with the flap motion. When the flap is up, the lift is higher and vice versa. However, the 1Hz case has some higher frequency content. Figure 19 shows pressure contours of the 1Hz case when the flap is near the top and bottom of its cycle. The low pressure spots are vortices being shed from the leading edge. Near the top of a cycle, strong vortices are shed from the leading edge and cause fluctuations in the lift coefficient as they pass over the airfoil. When the flap is down, fewer and weaker vortices are shed from the leading edge.

The case with a static flap angle of zero degrees showed that there were significant lift fluctuations as high as 3Hz. At a flapping frequency of 1Hz, these lift fluctuations have time to develop as the flap rotates up. The 5Hz case appears almost sinusoidal. One explanation is that the higher flap frequency does not allow time for the lower frequency lift fluctuations to form. While preventing these lower frequency fluctuations from forming improves airfoil stability, the 5Hz flapping motion makes large 5Hz lift fluctuations. A more practical consideration is that powerful actuators would be required to move the flap at this frequency. The added weight of actuators would degrade the overall aircraft performance.

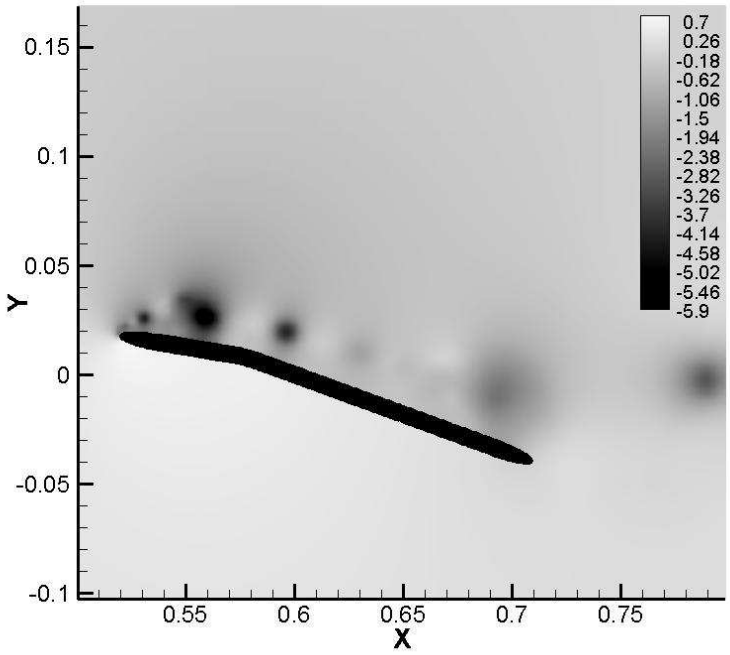

(a) Flap approaching the top of its cycle

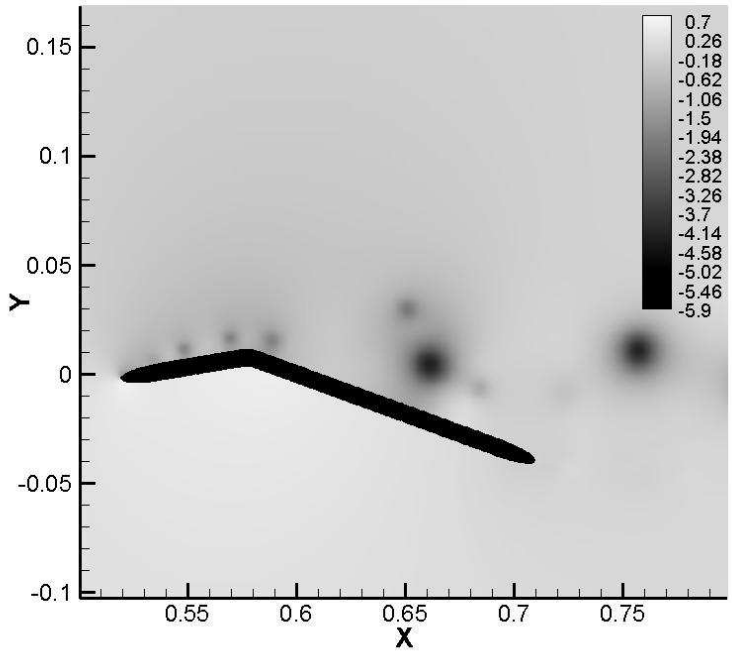

(b) Flap approaching the bottom of its cycle

Figure 19: Flapping airfoil at 1Hz at two different flap angles, α = 20°, Re = 14,700.

While this study has shown that a fictitious domain approach has promise to accurately predict the lift and drag properties of a thin airfoil, there is still a significant amount of numerical and experimental work that needs to be done before the numerical methods can be verified. However, the results can be used to guide further research. The addition of a front flap to a thin airfoil has the potential to greatly increase the performance of the airfoil. Additionally, moving the front flap has a large impact of the lift and drag of the airfoil. This effect depends on many factors including the frequency that vortices are shed from the leading edge.

REFERENCES

[1] Carmichael, B. H. “Low Reynolds Number Airfoil Survey.” Volume I, NASA Contractor Report 165803, November 1981.

[2] Kapsenberg, F., Shreeve, K., and Haley, D. “Low Reynolds Number Flight Control.” Oregon State University, School of Mechanical, Industrial, and Manufacturing Engineering. February 2009.

[3] Kapsenberg, F. “ME 406 Report.” Oregon State University, School of Mechanical, Industrial, and Manufacturing Engineering. March 2009.

[4] Broeren, A. P., and Bragg, M. B., 2001, “Unsteady Stalling Characteristics of Thin Wings at Low Reynolds Number,” Prog. Astronaut. Aeronaut., **195**, pp. 191-213.

[5] McCullough, G. B., and Gault, D. E., 1951, “Examples of Three Representative Types of Wing-Section Stall at Low Speeds,” NACA Technical Note 2502.

[6] Uranga, A., Persson, P., Drela, M., and Peraire, J. “Implicit Large Eddy Simulation of Transitional Flows Over Airfoils and Wings,” American Institute of Aeronautics and Astronautics, AIAA-2009-4131, June 2009.

[7] Schlüter, J. “Lift Enhancement at Low Reynolds Numbers using Pop-Up Feathers,” American Institute of Aeronautics and Astronautics, AIAA 2009-4195, June 2009.

[8] Taira, K. and Colonius, T. “Three-dimensional flows around low-aspect-ratio flat-plate wings at low Reynolds numbers,” Journal of Fluid Mechanics, **623**, pp. 187-207, 2009.

[9] Morse, D. R. and Liburdy, J. A. “Vortex Dynamics and Shedding of a Low Aspect Ratio, Flat Wing at Low Reynolds Numbers and High Angles of Attack,” Journal of Fluids Engineering, **131**, May 2009.

[10] Visbal, M. R., Gordnier, R. E., and Galbraith, M. C. “High-fidelity simulations of moving and flexible airfoils at low Reynolds numbers,” Experimental Fluids, **46**, pp. 903-922, March 2009.

[11] Apte, S. V., Martin, M., and Patankar, N. A. “A numerical method for fully resolved simulation (FRS) of rigid particle-flow interactions in complex flows,” Journal of Computational Physics, 228(8), pp. 2712-2738, 2009.

[12] Finn, J. “A Multiscale Modeling Approach for Bubble-vortex Interactions in Hydro-propulsion Systems,” M.S. thesis, Oregon State University, Corvallis, OR, 2009.

[13] Mittal, R., Dong, H., Bozkurttas, M., Najjar, F., Vargas, A., and von Loebbecke, A., 2008, “A versatile sharp interface immersed boundary method for incompressible flows with complex boundaries," Journal of Computational Physics, **227**(10), pp. 4825-4852.

[14] Marella, S., Krishnan, S., Liu, H., and Udaykumar, H., “Sharp interface Cartesian grid method I: An easily implemented technique for 3D moving boundary computations," Journal of Computational Physics, **210**(1), pp. 1-31, 2005.

[15] Henderson, R., “Details of the drag curve near the onset of vortex shedding," Physics of Fluids, 7, p. 2102, 1995.

[16] Shu, C., Liu, N., and Chew, Y., “A novel immersed boundary velocity correction-lattice Boltzmann method and its application to simulate flow past a circular cylinder," Journal of Computational Physics, **226**(2), pp. 1607-1622, 2007.

[17] Mittal, R. and Balachandar, S., “Effect of three-dimensionality on the lift and drag of nominally two-dimensional cylinders," Physics of Fluids, **7**, pp. 1841, 1995.

[18] Kravchenko, A., Moin, P., and Shari, K., “B-spline method and zonal grids for simulations of complex turbulent flows," Journal of Computational Physics, **151**(2), pp. 757-789, 1999.

APPENDICES

Appendix A – Grid for Flow Over A Cylinder

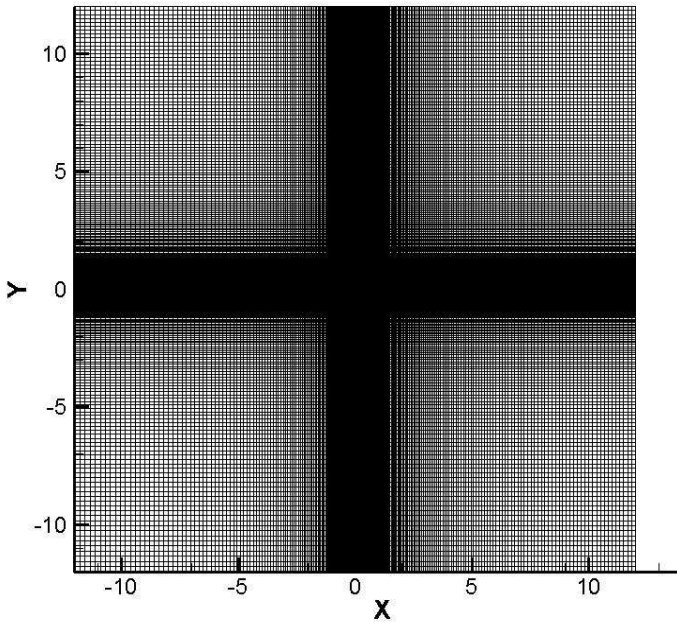

Figure A1: Grid for flow over a cylinder.

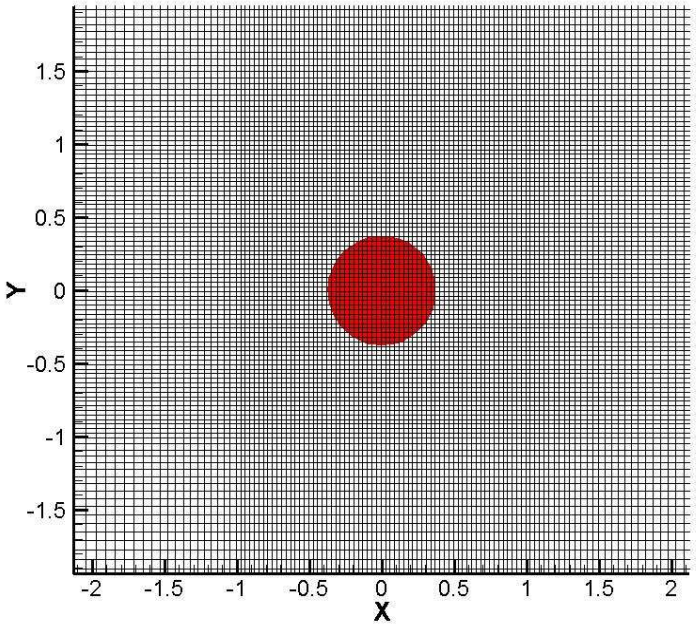

Figure A2: Cylinder cross-section and grid for flow over a cylinder.

Appendix B - Cylinder Grid Refinement Study Grid

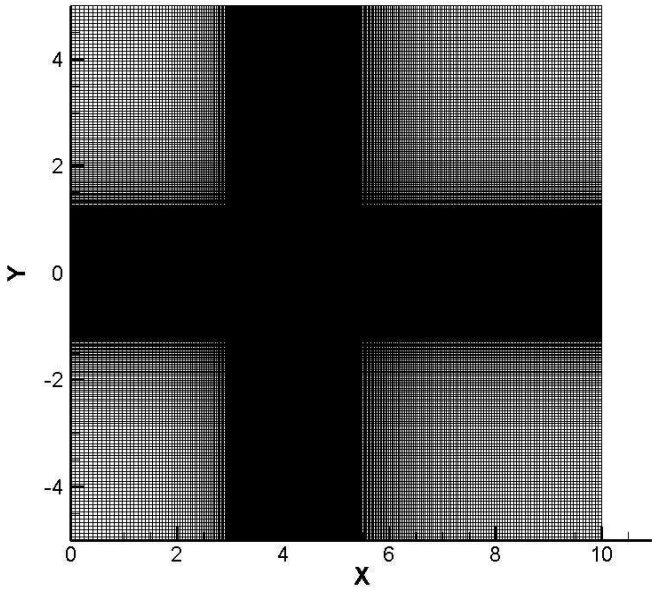

Figure B1: Fine grid for flow over a cylinder grid refinement study.

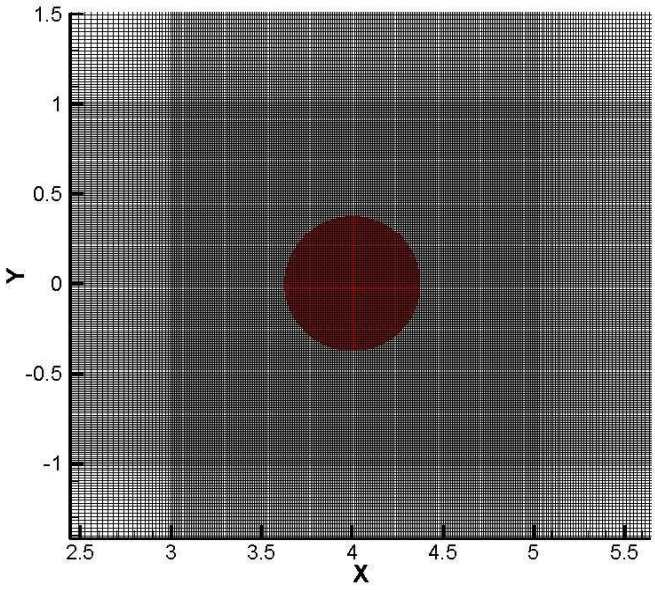

Figure B2: Cylinder cross-section using the fine grid for the flow over a cylinder grid refinement study.

Appendix C - Airfoil Grids

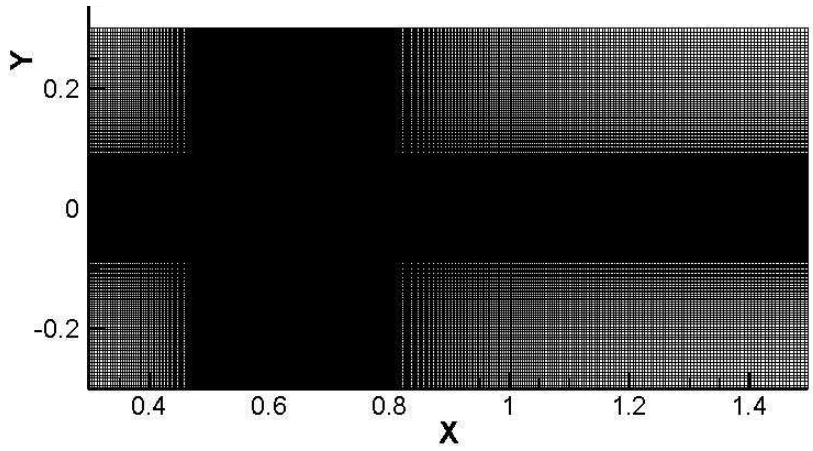

Figure C1: Coarse airfoil grid.

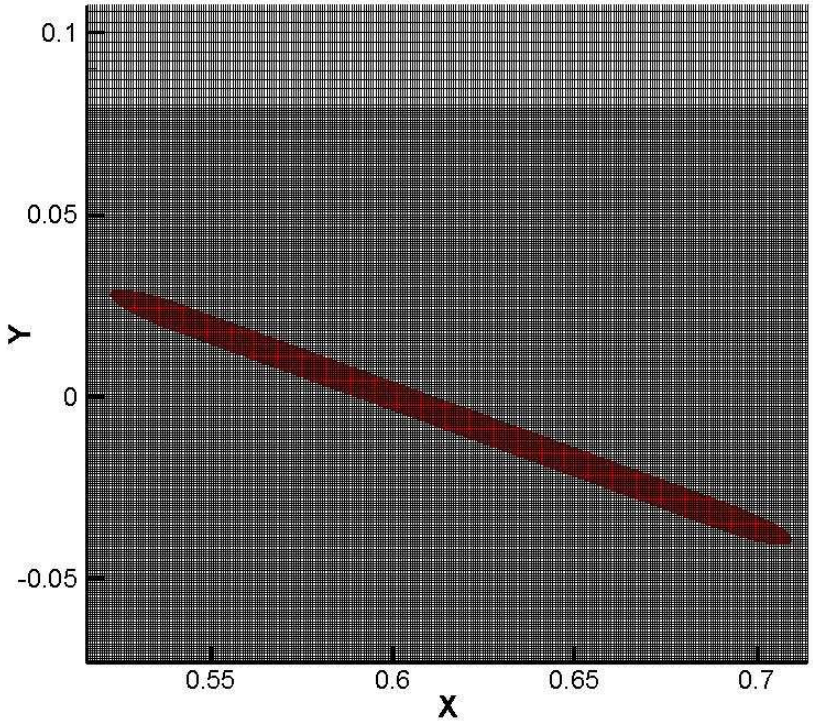

Figure C2: Airfoil cross-section on the coarse grid.

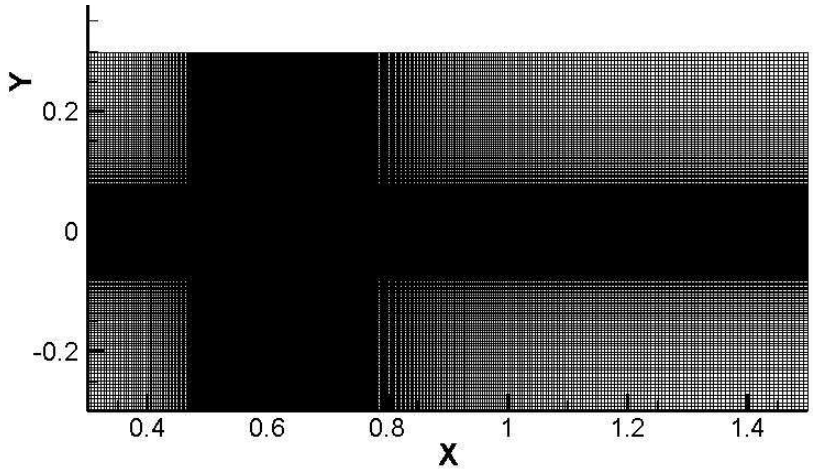

Figure C3: Intermediate airfoil grid.

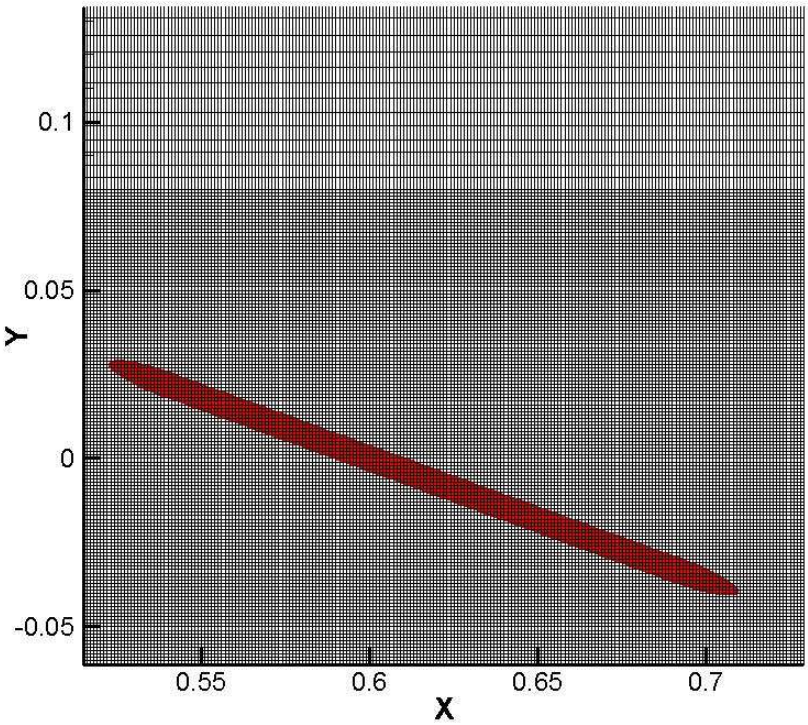

Figure C4: Airfoil cross-section on the intermediate grid.

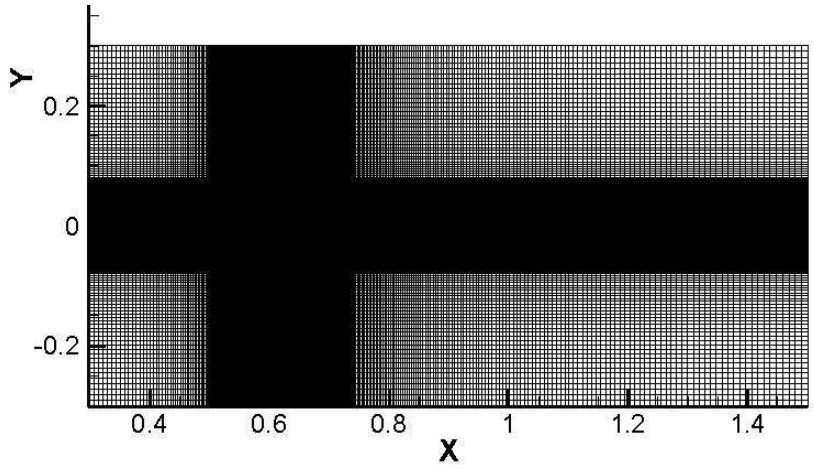

Figure C5: Fine airfoil grid.

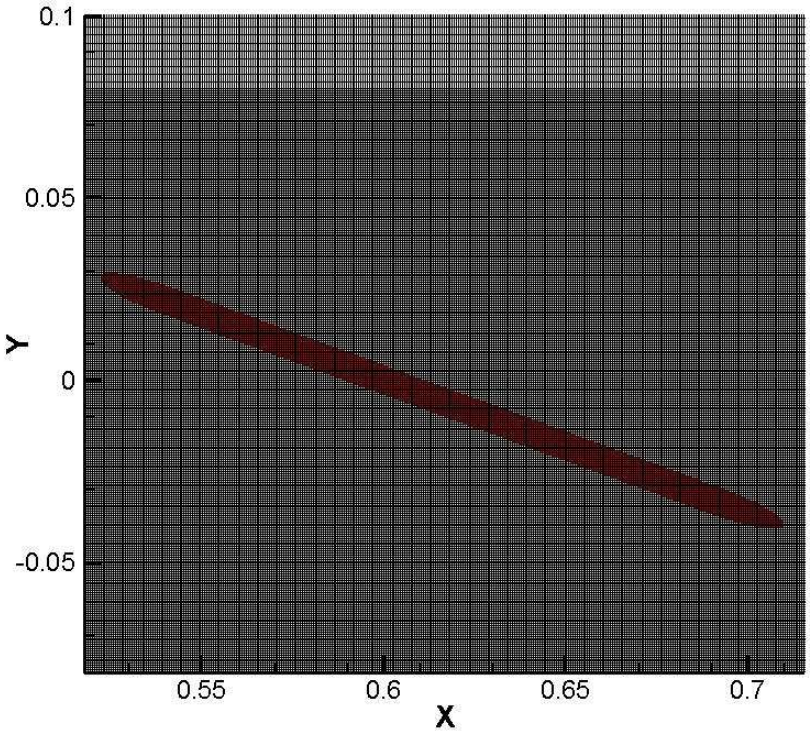

Figure C6: Airfoil cross-section on the fine grid.

Appendix D - Fixed Flap Angle Cases Drag Data

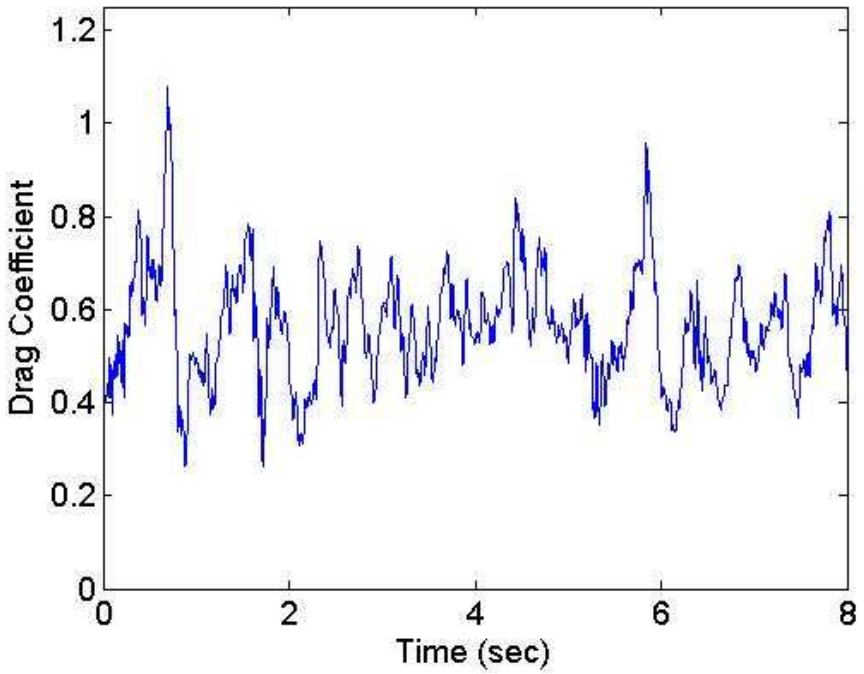

Figure D1: Coefficient of drag for the airfoil, α = 20°, θ = 0°, Re = 14,700. Average value = 0.56, varies between 0.96 and 0.26.

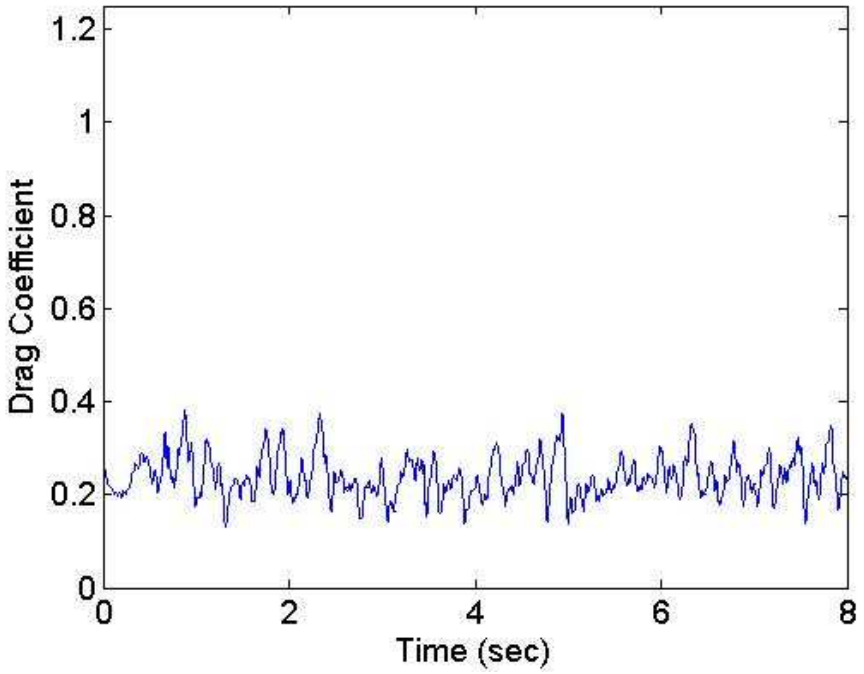

Figure D2: Coefficient of drag for the airfoil, α = 20°, θ = -20°, Re = 14,700. Average value = 0.24, varies between 0.37 and 0.13.

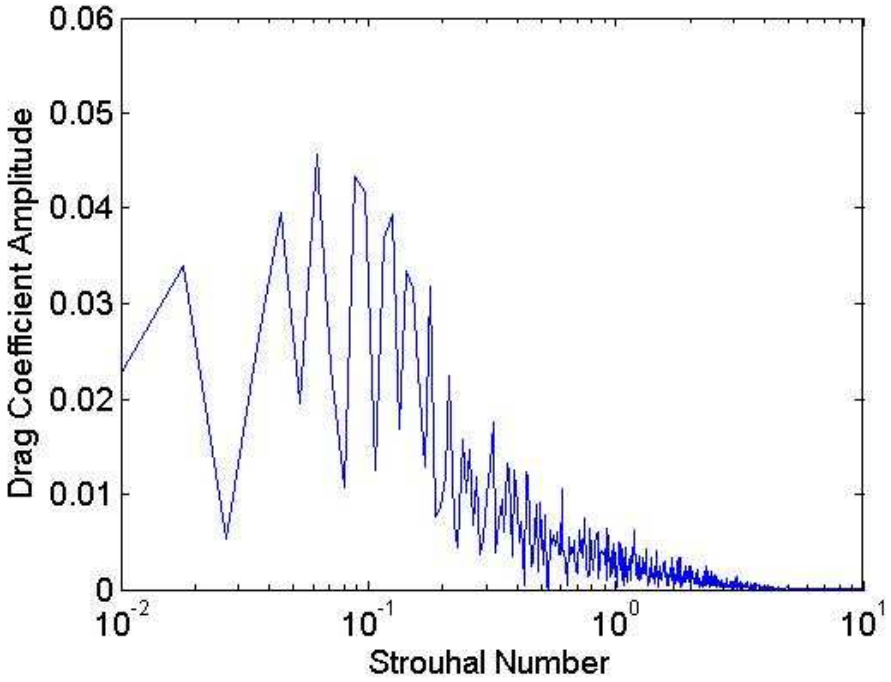

Figure D3: Spectral analysis of the coefficient of drag for the airfoil, α = 20°, θ = 0°, Re = 14,700. Peak Strouhal number = 0.062 with an amplitude of 0.046.

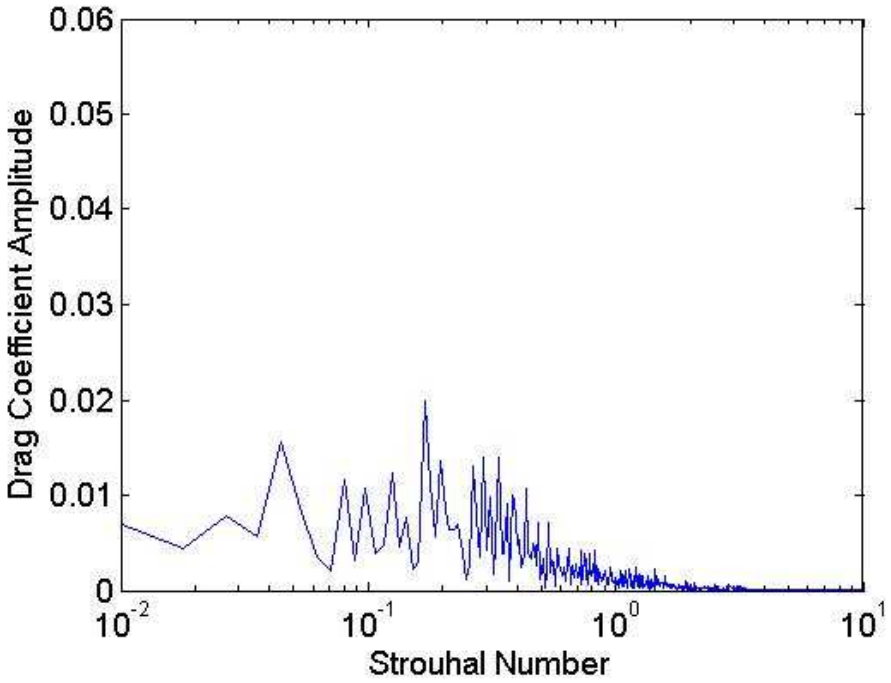

Figure D4: Spectral analysis of the coefficient of drag for the airfoil, α = 20°, θ = -20°, Re = 14,700. Peak Strouhal number of 0.17 with an amplitude of 0.020.

Appendix E - Flapping Cases Drag Data

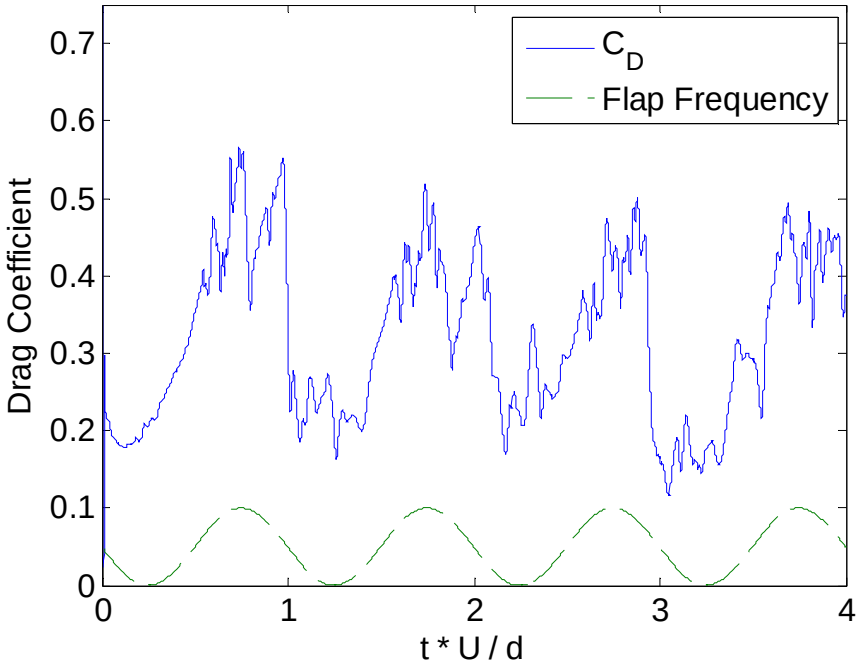

Figure E1: Coefficient of drag for the airfoil flapping at 1Hz, Re = 14,700. Average = 0.31, varies between 0.52 and 0.12.

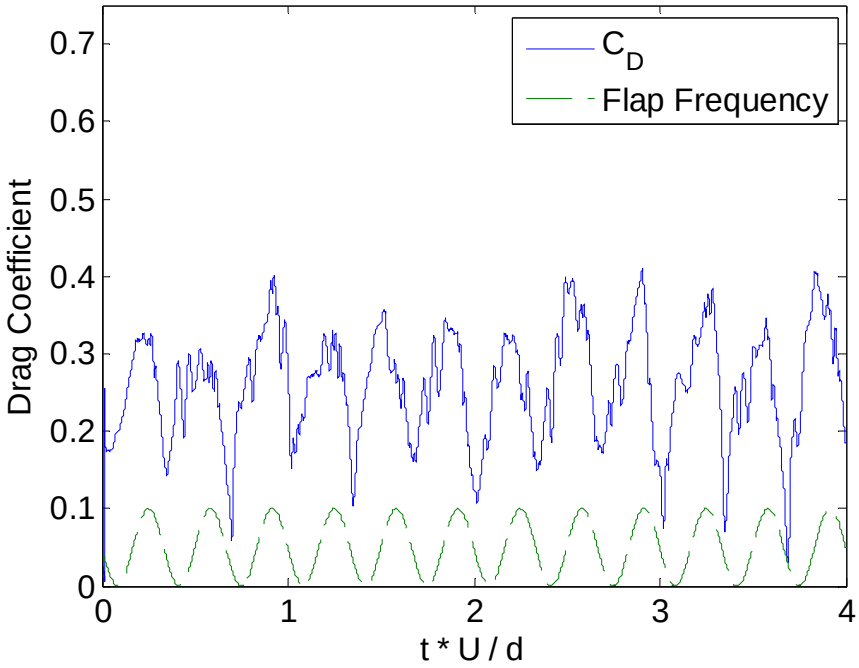

Figure E2: Coefficient of drag for the airfoil flapping at 3Hz, Re = 14,700. Average = 0.26, varies between 0.41 and 0.03.

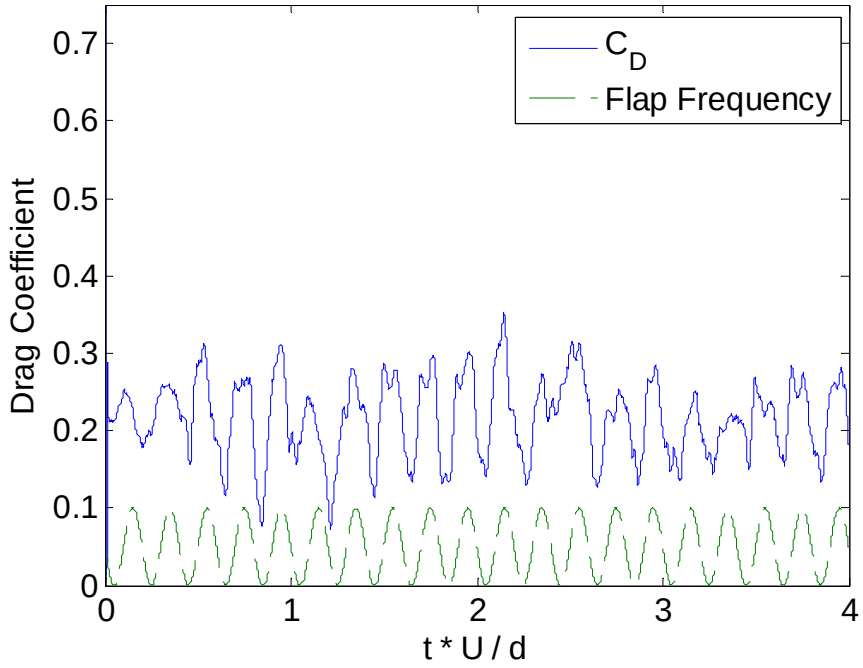

Figure E3: Coefficient of drag for the airfoil flapping at 5Hz, Re = 14,700. Average = 0.22, varies between 0.35 and 0.07.

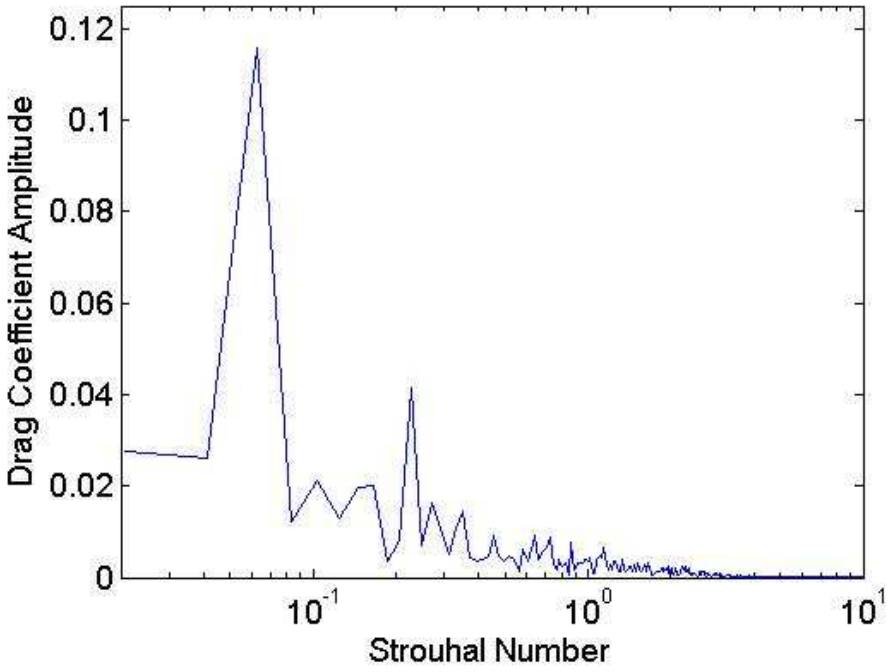

Figure E4: Spectral analysis of the coefficient of drag for the airfoil flapping at 1Hz, Re = 14,700. Peak Strouhal number = 0.062 with an amplitude of 0.12.

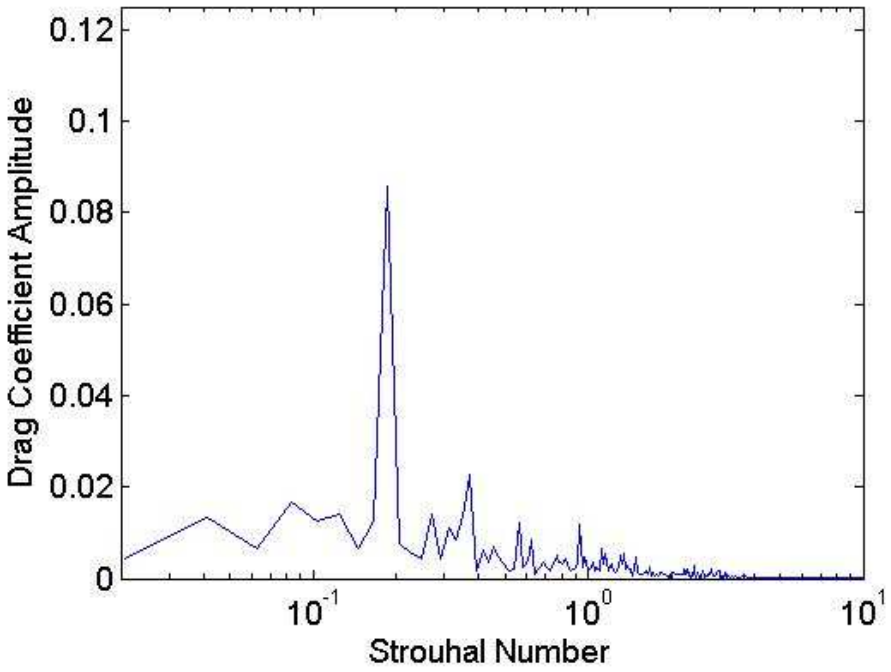

Figure E5: Spectral analysis of the coefficient of drag for the airfoil flapping at 3Hz, Re = 14,700. Peak Strouhal number = 0.19 with an amplitude of 0.09.

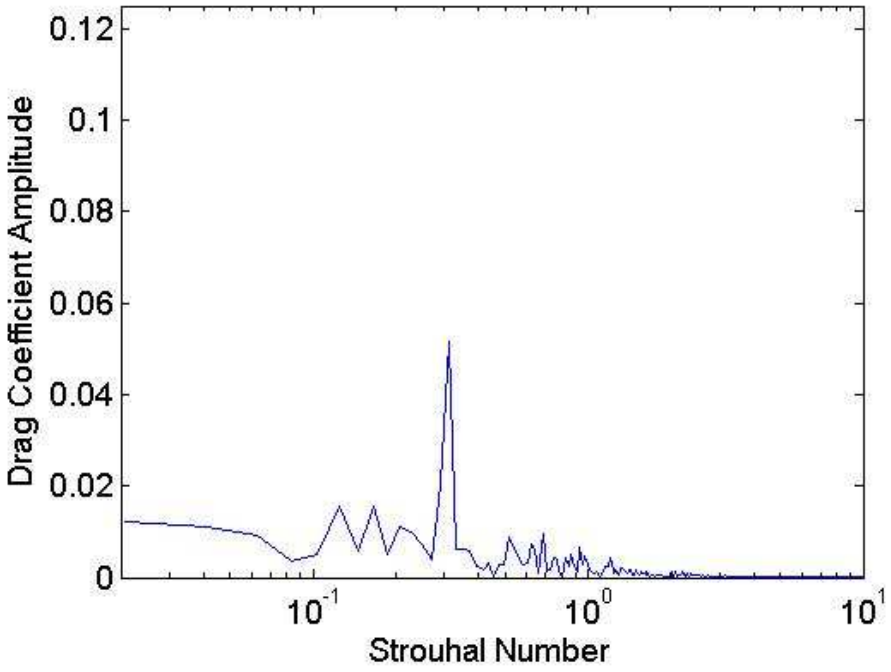

Figure E6: Spectral analysis of the coefficient of drag for the airfoil flapping at 5Hz, Re = 14,700. Peak Strouhal number = 0.31 with an amplitude of 0.052.